ANKARA YILDIRIM BEYAZIT UNIVERSITY

GRADUATE SCHOOL OF NATURAL AND APPLIED SCIENCES

PERFORMANCE OPTIMIZATION IN PBS QUANTUM DOT BASED INFRARED THIN-FILM PHOTODETECTORS

M.Sc. Thesis by

Irem SUTCU

Department of Energy Systems Engineering

June, 2022

ANKARA

PERFORMANCE OPTIMIZATION IN PBS QUANTUM DOT BASED INFRARED THIN-FILM PHOTODETECTORS

A Thesis Submitted to

The Graduate School of Natural and Applied Sciences of

Ankara Yıldırım Beyazıt University

In Partial Fulfillment of the Requirements for the Degree of Master of Science in Energy Systems Engineering, Department of Energy Systems Engineering

by

Irem SUTCU

June, 2022

ANKARA

M.Sc. THESIS EXAMINATION RESULT FORM

We have read the thesis entitled **"PERFORMANCE OPTIMIZATION IN PBS QUANTUM DOT BASED INFRARED THIN-FILM PHOTODETECTORS"** completed by **Irem SUTCU** under supervision of **ASSOC. PROF. DR. NURAY ÇELEBİ** and co-supervison of **ASSOC. PROF. DR. KUROŞ SALİMİ** and we certify that in our opinion it is fully adequate, in scope and in quality, as a thesis for the degree of Master of Science.

Assoc. Prof. Dr. Nuray ÇELEBİ

Supervisor

Assoc. Prof. Dr. Kuroş SALİMİ	Prof. Dr. Afife GÜVENÇ
Co-supervisor-Jury Member	Jury Member
Prof. Dr. Nuray YILDIZ	Asst. Prof. Dr. Sıtkı KOCAOĞLU
Jury Member	Jury Member

Prof. Dr. Sadettin ORHAN

Director

Graduate School of Natural and Applied Science

ETHICAL DECLARATION

I hereby declare that, in this thesis which has been prepared in accordance with the Thesis Writing Manual of Graduate School of Natural and Applied Sciences,

- All data, information and documents are obtained in the framework of academic and ethical rules,
- All information, documents and assessments are presented in accordance with scientific ethics and morals,
- All the materials that have been utilized are fully cited and referenced,
- No change has been made on the utilized materials,
- All the works presented are original,

and in any contrary case of above statements, I accept to renounce all my legal rights.

Date: Thesis defense date **Signature:…….**

Name Surname : Irem SUTCU

ACKNOWLEDGMENTS

I would like to take the opportunity to present my sense of gratitude to Dr. Itai Lieberman, and Dr. David Cheyns for giving me the opportunity to work in the group of Thin Film Photodetectors and well equipped IMEC laboratories. Special thanks go to Dr. Itai Lieberman, who has always inspired me with his deep knowledge, support that I have felt in every moment in IMEC, and invaluable guidance throughout this research.

I want to express my gratitude to Vladimir Pejovic. This thesis work would not have been successfully accomplished without his supervision and the valuable knowledge he gave me throughout the study.

I would like to thank Myung jin Lim for everything she taught me in the laboratory during my first days at IMEC and for helping me whenever I needed. I would also like to thank to all members of Thin Film Photodetector group.

I would like to sincerely gratitude to my supervisor Dr. Nuray Celebi and my co-supervisor Dr. Kourosuh Salimi for giving me support and help during the thesis studies.

I would never have been successful in this journey without the support and love of my family. I want to convey my love to my dear mother and my dear sister.

And my dear father, even though you are not alive now, I know that you are always here by me and the hand you put on my shoulder to support and guide me will stay with me forever.

2022, June 1st **Irem SUTCU**

PERFORMANCE OPTIMIZATION IN PBS QUANTUM DOT BASED INFRARED THIN-FILM PHOTODETECTORS

ABSTRACT

Because of its applications in areas ranging (e.g. remote sensing, cameras), imaging in the infrared (IR) range has garnered considerable attention. Photons in the short wave infrared (SWIR) range are less scattered by the particles in the atmosphere. As a result, SWIR light has strong penetrating qualities, allowing for sharp imaging even under poor weather conditions. Silicon, on the other hand, as significant in electronics, is commonly deployed in the industry for detection and imaging. However, because silicon's absorption capacity decreases dramatically beyond 1100 nm, imaging at SWIR requires alternate materials to be integrated atop silicon. Because of its size and tunable bandgap, solution-processable quantum dot (QD) photodetectors provide SWIR sensitivity. They are compatible with silicon substrates. They may be connected to silicon substrates utilizing low-cost and diverse technologies such as spin coating. However, in order to achieve good performance, QD photodetectors must have low dark current and high external quantum efficiency. To that aim, charge transport layers should be tuned properly since they play an important role in suppressing dark current.

In this thesis performance optimization was done by employing different hole transport layers and electron transport layers into the lead sulfide (PbS) quantum dot based photodetectors. Various characterization methods (e.g., external quantum efficiency-voltage/wavelength, current-voltage, absorbance measurements) were used to characterize fabricated devices that include novel transport layers. Followingly, best performing materials as transport layers were used in the structure of the photodetector which is on a silicon substrate that mimics CMOS ROIC structure. As a final step, studies were carried out to thin the absorber layer in order to reduce the cost of the product and make the production process easier.

Key words: SWIR, EQE, dark current, transport layers, photodetectors, QD

PbS KUANTUM NOKTACIK ICEREN INCE FILM FOTODEDEKTORLERDE PERFORMANS OPTIMIZASYONU

ÖZ

Kızılötesi (KÖ) bölgesinde görüntüleme, uzaktan algılama, kameralar gibi çeşitli alanlardaki uygulamaları nedeniyle büyük bir ilgi görmüştür. Kısa dalga kızılötesi (KDKÖ) aralığındaki fotonlar, atmosferdeki parçacıklar tarafından daha az saçılır. Sonuç olarak, KDKÖ ışığı güçlü nüfuz etme özelliklerine sahiptir ve kötü hava koşullarında bile keskin görüntülemeye olanak tanır. Öte yandan, elektronikte önemli olan silikon, algılama ve görüntüleme için endüstride yaygın olarak kullanılmaktadır. Bununla birlikte, silikonun absorpsiyon kapasitesi 1100 nm'nin üzerinde önemli ölçüde azaldığından, KDKÖ'de görüntüleme, silikonun üzerine entegre edilecek alternatif materyaller gerektirir. Boyutu ve ayarlanabilir bant aralığı nedeniyle, çözümle işlenebilir kuantum nokta (KN) fotodedektörler, KDKÖ duyarlılığı sağlar. Silikon substratlarla uyumludurlar. Döndürerek kaplama gibi düşük maliyetli ve çeşitli teknolojiler kullanılarak silikon substratlara bağlanabilirler. Ancak, iyi performans elde etmek için KN fotodedektörlerin düşük karanlık akıma ve yüksek harici kuantum verimliliğine sahip olması gerekir. Bu amaçla, yük taşıma katmanları, karanlık akımı bastırmada önemli bir rol oynadıkları için uygun şekilde ayarlanmalıdır.

Bu tezde, kurşun sülfat (PbS) kuantum nokta tabanlı fotodedektörlere farklı delik taşıma katmanları ve elektron taşıma katmanları kullanılarak performans optimizasyonu yapılmıştır. Yeni taşıma katmanları içeren fabrikasyon cihazları karakterize etmek için çeşitli karakterizasyon yöntemleri (örneğin, harici kuantum verimliliği-voltaj/dalga boyu, akım-voltaj, absorbans ölçümleri) kullanıldı. Daha sonra, CMOS ROIC yapısını taklit eden bir silikon altlık üzerinde, fotodedektörün yapısında taşıma katmanları olarak en iyi performans gösteren malzemeler kullanılmıştır. Son aşama olarak, ürünün maliyetini düşürmek ve üretim sürecini daha kolay hale getirmek için emici tabakanın inceltilmesine yönelik çalışmalar yapılmıştır.

Anahtar kelimeler: KDKÖ, EQE, karanlık akım, iletim katmanları, fotodedektörler, KN

CONTENTS

NOMENCLATURE

Symbols

V_{bi}	Built-in Potential Barrier
V_R	Reverse Bias Voltage
E_{app}	Electric Field
I_{dark}	Dark Current
D*	Detectivity
I_s	Reverse Saturation Current
h	Planck's Constant
c	Speed of Light
q	Charge
I_{sh}	Shot Noise
I_{th}	Thermal Noise
W	Space Charge Width
E_g	Energy Gap
λ	Wavelength
N_A	Acceptor Concentration
N_D	Donor Concentration
R	Responsivity

Acronyms

IR	Infrared
NIR	Near Infrared
SWIR	Short Wave Infrared
MWIR	Medium Wave Infrared
LWIR	Long Wave Infrared
CMOS	Complementary Metal Oxide Semiconductor
UV	Ultraviolet
CQD	Colloidal Quantum Dot
ROIC	Readout Integrated Circuit
CCD	Charge-Coupled Device

QDPD	Quantum Dot Photodetector
EQE	External Quantum Efficiency
IQE	Internal Quantum Efficiency
NEP	Noise Equivalent Power
SNR	Signal to Noise Ratio
DOS	Density of States
HTL	Hole Transport Layer
ETL	Electron Transport Layer
InGaAs	Indium Gallium Arsenide
HgCdTe	Mercury Cadmium Telluride
Cu	Copper
TiN	Titanium Nitride
PbS	Lead sulfide
PolyTPD	Poly (N, N'-bis-4-butylphenyl-N ,N'-bisphenyl)Benzidine
NiO_x	Nickel Oxide
2PACz	2-(9H-Carbazol-9-yl)ethyl] phosphonic
BDT	1,4 benzene dithol
ZnI_2:MPA	Zinc Iodide with 3-Mercaptopropionic Acid
ZnO:Mg	Magnesium Doped Zinc Oxide
C_{60}	Buckminsterfullerene
TiO_2	Titanium Dioxide
PVD	Physical Vapor Depositions
Al	Aluminum
ITO	Indium Tin Oxide
MoO_x	Molybdenum Oxide

LIST OF FIGURES

CHAPTER 1

INTRODUCTION

Detection in the infrared (IR) region has received great attention for various fields in recent years, such as optical fiber communications, imaging, food inspection, remote sensing, medical imaging. For this reason, many research groups has been studying on the IR region of the electromagnetic spectrum. IR region splits into categories; near-IR (NIR) (0.75-1.4 μm), short-wave-IR (SWIR) (1.4-3 μm), medium-wave-IR (MWIR) (3-8 μm), long-wave-IR (LWIR) (8-15 μm) [1]. However, the same wavelengths can be named differently in different fields of studies. For example, 1.55 μm wavelength is normally accepted in the SWIR region in the defense industry, while it is accepted in the NIR region in the studies of astronomy. Atmospheric transparency is high in the MWIR and LWIR regions, resulting in good transmission with little loss. Therefore, these regions are important for astronomy and free-space communication [2].

Compared to visible light, SWIR has a stronger penetrating ability to atmospheric particles by scattering less from dense particles such as dust and fog. This also enables to capture clear images even in bad weather conditions (e.g., hazy, and smoky) as well as night-time imaging. Meanwhile, SWIR can easily distinguish cold background objects with minimal loss [3, 4].

Silicon-based complementary metal-oxide-semiconductor (CMOS), known as one of the technological revolutions, is crucial for image sensors. However, the absorption coefficient of silicon decreases sharply beyond the wavelength of 1100 nm. It is a barrier to various applications such as light-gathering, communication, and sensing. To address this issue, compound semiconductors such as InGaAs and HgCdTe are used in these structures, as their low energy band gaps allow sensing longer wavelengths [5, 6, 7]. These materials are grown separately by using the epitaxial growth techniques followed by flip-chip bonding of the processed photodetector arrays to silicon readout circuits (ROICs) (figure 1.1a). This non-monolithic (hybrid) approach increases the cost of the process along with rising incompatibility issues

during the bonding process on CMOS. Furthermore, the size of the bumps restricts the minimum achievable spacing between each pixel, known as pixel pitch, to the smallest state-of-the-art pixel pitch of 5 μm at the moment of writing this thesis [8]. These reasons make many research groups to investigate new materials for SWIR photodetectors [6, 9, 10, 11].

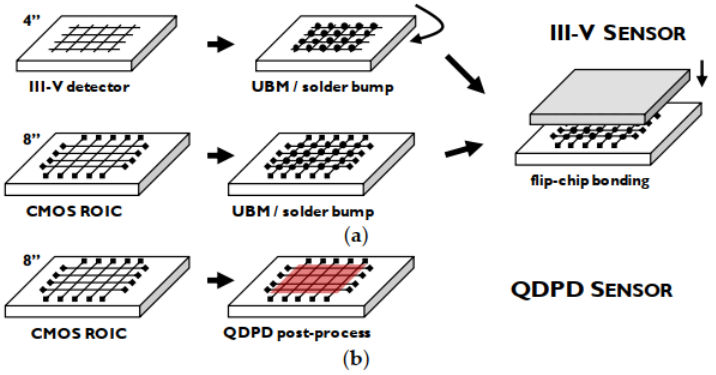

Figure 1. 1 Flip-chip bonding process of commercial IR materials on CMOS ROIC (a) CQD monolthic integration on CMOS ROIC [6]

Colloidal quantum dots (CQDs) with attractive properties such as photon absorption tunability from ultraviolet (UV) to infrared (IR), thanks to their size-tunable bandgap have emerged as new material for IR detectors. Furthermore, bulk properties, mobility, doping level, carrier concentration and lifetime of CQDs may finely be tuned by varying the shape, surface chemistry and size of the material, allowing for significant diversity for photodetector design and subsequent integration on readout integrated circuits (ROICs) [12].

CQDs such as lead chalcogenide (PbE, E = S, Se, Te), mercury chalcogenide (HgE, E = S, Se, Te), and silver chalcogenide (Ag_2E, E = S, Se, Te) are alternative to traditional bulk IR semiconductors with their broad IR absorption and good carrier transport properties. Moreover, they can be deposited by simple solution-based deposition methods which enables monolithically application onto CMOS ROIC (figure 1.1b) [12].

CQDs attract attention with their easy, low-cost, and solution-based fabrication methods. Moreover, they are compatible with flexible substrates [13].

In addition, it is possible to integrate other materials with CQDs to reduce surface defect density, increase carrier mobility, , and increase their lifetime. By optimizing the device, carrier separation, extraction-transportation can be changed [12].

In this thesis, studies were carried out to optimize photodetector performance by adding different transport layer materials. Several materials have been tested to decrease the dark current, and to increase external quantum efficiency (EQE) as much as possible. In the first stage, experiments were carried out on glass substrates, which is a cost-effective way to manufacture lead sulfide (PbS) QD based thin film photodetectors (TFPDs). Here, several transport layers were tested. Furthermore, in the second stage, the best performing transport layers from the first stage were used in the photodetector structure with silicon substrate which has bottom contacts mimicking the CMOS ROIC design. In addition, as a final step, studies on thinner QD absorber layers have been done to get more fab-friendly, less expensive, and easy production. Furthermore, an anti-reflective layer was applied to the silicon substrate in the stack design which has thinner absorber layers. The device performances were investigated by using different characterization methods.

CHAPTER 2

LITERATURE REVIEW

2.1 Doped Semiconductors

Semiconductors incorporated with foreign atoms are called doped (extrinsic) semiconductors. Intrinsic semiconductors have a low concentration of charge carriers also, their electrical properties are sensitive to defects and chemical impurities. However, doping of the semiconductor allows for increasing concentration of the carriers with a controlled way of intrinsic semiconductors (figure 2.1).

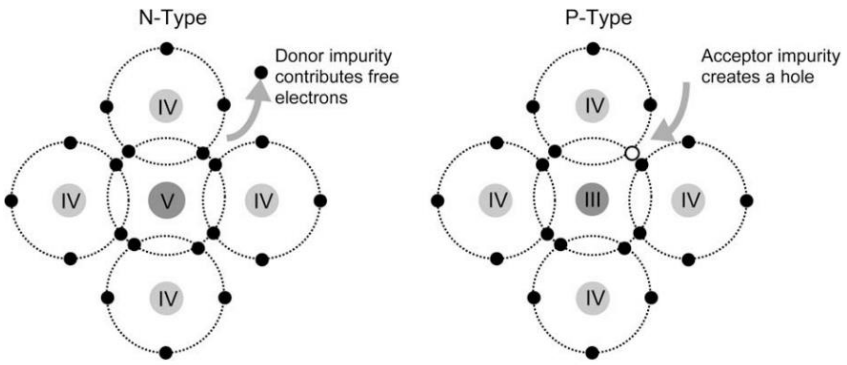

Figure 2. 1 n-doped and p-doped semiconductors[15]

Since silicon and germanium are the fourth group element, they have four electrons on their outer shell. If the atoms from the fifth group of the periodic table incorporate into the lattice of silicon or germanium, like phosphorus or arsenic, there will become an excess carrier. This extra carrier can contribute to the electrical conduction by transferring to the conduction band of silicon or germanium, thanks to its thermal energy. Then the phosphorus or the arsenic atom will be positively ionized. These atoms from the fifth group are called donor atoms. It is possible to dope silicon or germanium atoms with the third group elements. Having considered the same idea, aluminum or gallium atoms have three electrons on the outer shell can incorporated into the lattice of silicon or germanium. In this concept, there will be one missing electron. This missing electron can fill with the electron at the valance band has enough

thermal energy. These atoms from the third group are called acceptor atoms [14,15, 16].

2.2 p-n Junction

In modern technology, p-n junction is a building block for semiconductor devices such as, light emitting diodes, lasers, and transistors. Most of the devices that are produced with semiconductor technology include at least one junction between oppositely doped semiconductor regions. For this reason, it is crucial to create a proper p-n junction with an appropriate characterization for a high performing device [17].

An idealized model of the p-n junction is when one side of the junction has uniformly and purely p-type doped material with an acceptor concentration N_A and the other side has uniformly and purely n-type doped material with a donor concentration N_D. The interface between the p and n regions is known as the metallurgical junction. To make it simple, if we consider a step junction where the doping concentration in each section is uniform and the doping concentration abruptly changes at the junction, at first there is a substantial density gradient in both regions at the metallurgical junction. The n region majority carrier electrons will start diffusing into the p-region, while the p-region majority carrier holes will start diffusing into the n-region. However, the motion state of the charges does not continue indefinitely if there are no external connections. Positively charged holes are left behind as electrons diffuse from the n region and vice versa. At the end of this motion, there is an electric field induced by positive charges and negative charges in the regions around the metallurgical junction. Negatively charged p-region and positively charged n-region form the space charge region as shown in figure 2.2.

If there is no applied voltage throughout the p-n junction, the junction will be in thermal equilibrium, with the Fermi energy level remaining constant across the system (figure 2.3.). Because the positions of the valance and conduction bands with respect to the Fermi energy shifts between the p and n regions, the energy levels of conduction and valance bands must bend as we move through the space charge region.

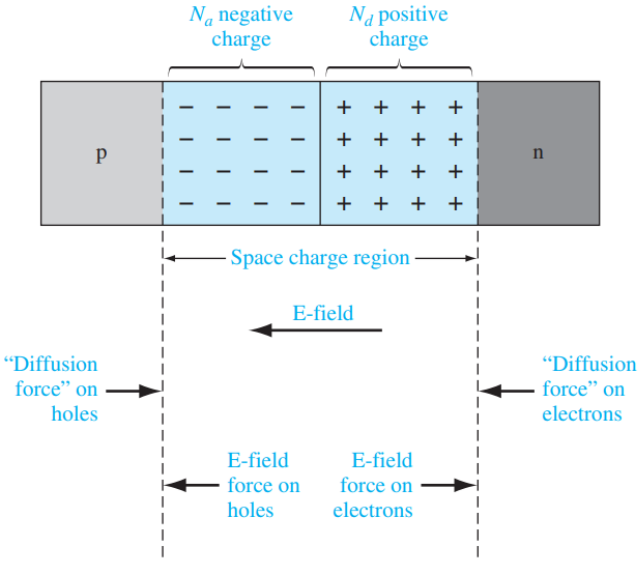

Figure 2. 2 The space-charge region and the electric field [16]

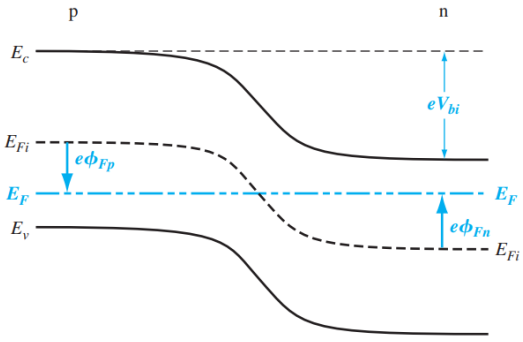

Figure 2. 3 Fermi level of the p-n junction in thermal equilibrium [16]

When the conduction band electrons of n region try to travel through the conduction band of p region, they encounter a potential barrier. This potential barrier known as built-in potential barrier indicated by V_{bi}.

There will not be an equilibrium condition anymore if there is a potential applied between the p and n region. Furthermore, fermi level of energy is not constant throughout the system.

Under reverse bias, there is positive bias applied to the n region of the p-n junction (figure 2.4b). Figure 2.4a shows how energy band diagram changes when a p-n junction operated under reverse bias voltage regime. The fermi level of the n side is lower than the fermi level of the p side because the positive potential is downward (figure 2.4a). However, the applied voltage is equal to the energy difference between them. At the end of this process there is an increased total potential barrier (figure 2.4b), V_{total} is given by,

$$V_{total} = |\varphi_{Fn}| + |\varphi_{Fp}| + V_R \quad \textbf{(2.1)}$$

where applied reverse bias voltage is indicated with V_R.

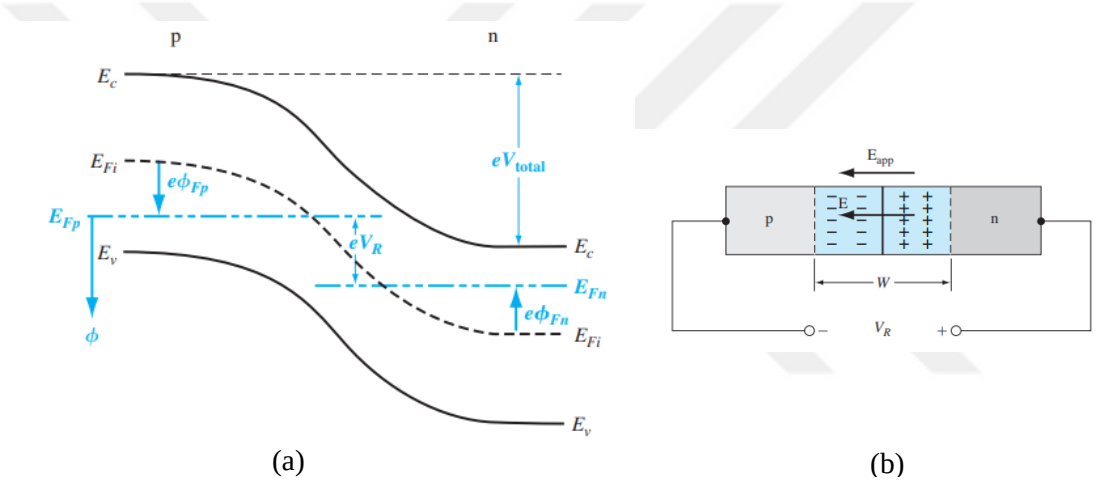

Figure 2. 4 Energy-band diagram under reverse bias (a) p-n junction operated under reverse bias voltage (b) [16]

The potential barrier is reduced when a positive voltage, V_a, is applied to the positive side (figure 2.5a). Figure 2.5b shows how energy band diagram of the p-n junction changes under forward bias. In the bulk p and n areas, the electric field is generally quite small. Almost all of the voltage is applied across the junction. The applied voltage induces the electric field E_{app} that is in the opposite direction of the space-charge electric field, lowering the net electric field in the space charge region below its equilibrium value [16].

2.3 Heterojunction

In the previous section it was assumed that all throughout the structure the of the semiconductor material is homogeneous. This type of junction is known as homojunction. However, if the junction forms between two distinct semiconductors this junction is known as heterojunction. Different bandgap energies of different semiconductor materials will lead to energy band discontinuities at the interface of the junction. When the junction shifts abruptly from narrow to wide bandgap, there may occur an abrupt junction. Properly matched lattice constants are crucial to be able to get a well performing heterojunction. Furthermore, lattice mismatch may cause dislocations in interfaces.

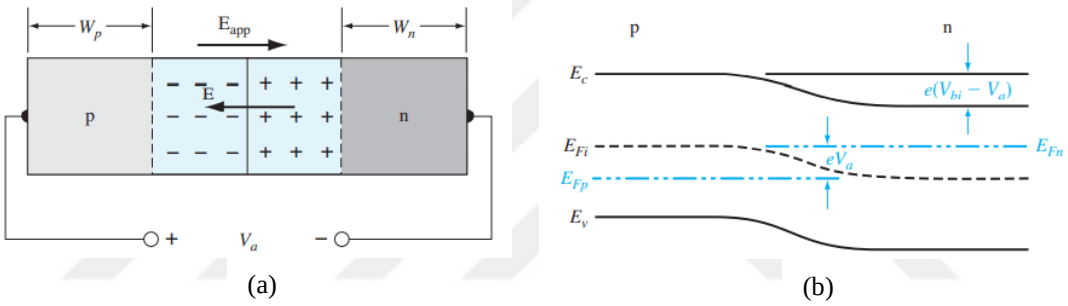

Figure 2. 5 Energy-band diagram under forward bias (a) p-n junction operated under forward bias voltage (b) [16]

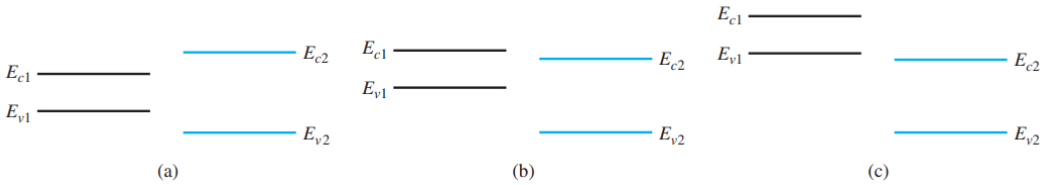

Figure 2. 6 Junction formation between a wide and a narrow bandgap material, straddling (a), staggered (b) and wide band gap (c) [16]

During the junction formation between a wide and a narrow bandgap material, band alignment between these materials is crucial since it determines the characteristics of

the heterojunction. As shown in the figure, there are three different situations arise during the junction between wide and narrow bandgap materials; straddling, staggered and wide band gap.

2.4 Photodetectors

Few research fields have contributed as much to unravel the mysteries of the Universe as the study of the interaction of light and matter, which has resulted in many breakthroughs scientific discoveries.

The interaction of light, particularly with semiconducting materials, has allowed us to understand the behavior of several fundamental phenomena. Also, it has created the groundwork for today's optoelectronic devices. The majority of these systems require light detection, which is accomplished via photodetector devices [18].

Incoming radiation is converted into electrical signals by photodetectors. An absorber semiconductor material absorbs incoming light in a photodetector device, after which the photons form electron-hole pairs. This phenomenon produces modulated electrical current as the photodetector output with the help of an external or built-in electric field. Photodetectors are essential components of sensing, optical imaging, and communication systems [19]. Typically, the detecting capacity of incoming radiation can be substantially evaluated by monitoring the device's voltage or current signal [20].

Photodetectors are crucial for communication applications, imaging, and sensing. Photodetectors can be categorized into different categories due to their operating wavelength range such as IR photodetectors, UV (ultraviolet) photodetectors, x-ray photodetectors. In the medical field, x-ray photodetectors are commonly used. CMOS (Complementary Metal Oxide Semiconductor) and CCD (Charge-coupled Device) are commonly used photodetectors in the category of visible photodetectors which are used in digital cameras and smartphones commonly. Inorganic semiconductors have dominated commercial optoelectronic devices, including photodetection devices. However, the high cost of these established mature inorganic semiconductor-based photodetectors, difficult manufacturing procedures, and lack of mechanical flexibility

have hindered mass production and integration with innovative technologies [19]. Semiconductor-based organic photodetectors have advantages over inorganic semiconductors. Such as mechanical flexibility, producibility in large areas, solution-based and low-cost fabrication methods. However, a limited life span and slower time of operation are the drawbacks of organic semiconductor-based photodetectors. Therefore, inorganic semiconductors are widely used materials in commercial optoelectronic devices [20, 19, 16].

2.6 Photodiodes

Photodiodes are the most common photodetector type which compose of p-n junction diodes that generally operated under a reverse bias voltage. They have several types of structures, such as PIN photodiodes that have junctions between p-type, –intrinsic– n-type materials, PN junction photodiodes that have junction between oppositely doped semiconductors, Schottky junction photodiodes that have junction between the metal electrodes and a doped, heterojunction photodiodes that have one or more than one blocking junctions between semiconductors (intrinsic) or junctions between semiconductors(intrinsic) and metals and avalanche photodiodes.

The presence of the electric field in the junction allows the photogenerated carriers to be separated and the electrons and holes to be effectively driven to the opposing contact electrodes. Because photodiode response time is determined by the carrier's travel time to the corresponding electrode, semiconductors with high carrier mobility are frequently associated with high bandwidth operation. The maximum principal quantum efficiency of conventional photodiodes is 100% due to the junction potential barrier that prevents charge carrier recirculation. That is to say it cannot produce gain and the improvement of signal strength is limited. However, photodiode dark current benefits from barrier of the junction, since only a few hot carriers can cross through the junction and create extremely low dark current, resulting in a high SNR. Multiple carriers can be formed per single photon by using an avalanche or carrier multiplication mechanism [10].

The electric field quickly sweeps the excess carriers created inside the space charge zone out of the depletion region; negative charges are swept quickly into the n region,

and positive charges into the p region. The current density generated by photon from the space-charge region is shown in equation 2.5,

$$J = e \int G \, dx \tag{2.5}$$

where the integral is over the width of the space charge region. If G is constant then in equation 2.6,

$$J = eGW \tag{2.6}$$

where W indicates the space charge width. However, the direction is reverse- biased for J here. This characteristic of photocurrent has very fast response to the photon illumination called prompt photocurrent [16, 21].

2.5 Figures of Merit

Photodetectors have several important figures of merit. These are, dark current ($I_{dark,}$), external quantum efficiency (EQE), noise equivalent power (NEP), detectivity (D*), and bandwidth.

Dark Current (I_{dark}) is basically the constant current which exist under dark conditions. Because photodiode maintained under reverse bias, the reverse saturation current (I_s) the same with the dark current.

Band-to-band, generation- recombination current, trap-to-band mechanisms the are the main sources of the dark current in a photodetector [22][23][24].

External quantum efficiency (EQE) is calculated by dividing the number of generated charge carriers in the device to the number of incident photons. There is a relation between responsivity, photoconductive gain, EQE as shown in equation 2.2,

$$\text{EQE}\ (\lambda) = \ R(\lambda)\frac{hc}{q\lambda} \approx R(\lambda)\frac{1.24}{\lambda} \tag{2.2}$$

where, h is the Planck's constant, c is the speed of light and the charge is shown by q.

Noise equivalent power (NEP) is the minimum measurable power. Noise equivalent power (NEP(λ)) is the optical power where the signal-to-noise ratio (SNR) achieves the unity. NEP can be defined by equation 2.3,

$$\text{NEP}\ (\lambda) = \frac{\sqrt{I_n^2}}{R(\lambda)} \tag{2.3}$$

where the noise current spectral density is shown by I_n, responsivity is shown by R.

In a photodetector the current of total noise is the summation of the noise sources; shot noise (I_{sh}), thermal noise (I_{th}), low-frequency flicker noise (1/f).

SNR is one of the important parameters since it determines the signal system quality. There must be a low noise level and a high responsivity in a photodiode to achieve a high SNR.

Detectivity (D*) is the one of the crucial figures of merit of photodetectors. It allows to compare photodetectors via different structures and areas. Detectivity is equal to signal-noise ratio (SNR), if there is 1 cm^2 of device area, 1 Hz of detection bandwidth and 1 W of incident power. Detectivity (D*) is given by equation 2.4,

$$D^*(\lambda) = \frac{\sqrt{A}}{NEP(\lambda)} \tag{2.4}$$

where A is area, NEP is noise equivalent power.

As photodetector detectivity is directly contingent upon the responsivity, the detectivity is indirectly a function of the applied electric field, the function of wavelength, and modulation frequency [22].

Response time (τ) is the time it takes for the detector output to change in response for changing the input light intensity. This is an important feature of any photodetector.

The p-n junction, which acts as a barrier to the flow of majority carriers in photodiode detectors, suppresses the replenishing process. Because the time it takes for charge carriers to traverse through the high-field zone of the junction (the carrier transit time)

can be much less than the carrier lifespan, the response time is significantly enhanced [25, 12].

2.7 CQDs and CQD Photodetectors

CQD photodetectors gained a considerable improvement in the last decade and significant progress has been made in the development of CQDs. Their possible advantages include, inexpensive and simple manufacture, direct coating on silicon for imaging, and size-tunable throughout a large infrared spectral region, and direct coating on silicon circuits for imaging, which possibly decreases array cost and provides additional modifications such as flexible infrared detectors. Wave functions of electrons and holes may be comparable the dimensions of the device structure. This implies that electrical engineering can be done at the quantum-mechanical level. The carrier energy spectrum can be changed significantly by the electron confinement of a semiconductor material. Electron confinement can arise novel physical properties. A variation in density of states (DOS) results in the majority of expected improvements in optoelectronics. Figure 2.7 shows the comparison of DOSs and carrier distribution for bulk and dot materials.

Conduction band minimum and the valance band maximum that have an energy gap (E_g) between them, determines the optical and transport property. However, if there is a confinement in each tree-dimensions, the valance band and the conduction band energy states become discrete. Furthermore, it gains size dependent band gap property.

CQDs are promising materials with their size-tunable bandgaps, cheap and easy synthesis by liquid-phase method, and solution processable deposition techniques. Furthermore, they can be monolithically applied on ROICs. Several studies have done to reduce the production cost and scale up the performance of the CQD. Colloidal solution-phase synthesis is the most prevalent method for fabricating colloidal infrared QDs.

Long oleic acid molecules are the most commonly used ligand type during the synthesis process. However, reducing the tunnel barrier of the dots is crucial to obtain a conductive CQDs. Long oleic acid ligand molecules are usually changed by the

methods, solid state ligand exchange and solution-phase ligand exchange. During the ligand exchange process long ligand molecules are changing with the short ones to reduce interparticle spacing and increase the conductivity.

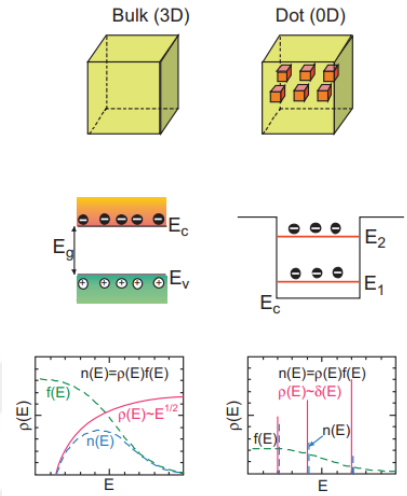

Figure 2. 7 DOS and carrier distribution for bulk(3D) (a) and QD (0D) (b) [26]

CQDs are promising materials with their size-tunable bandgaps, cheap and easy synthesis by liquid-phase method, and solution processable deposition techniques. Furthermore, they can be monolithically applied on ROICs. Several studies have done to reduce the production cost and scale up the performance of the CQD. Colloidal solution-phase synthesis is the most prevalent method for fabricating colloidal infrared QDs.

Long oleic acid molecules are the most commonly used ligand type during the synthesis process. However, reducing the tunnel barrier of the dots is crucial to obtain a conductive CQDs. Long oleic acid ligand molecules are usually changed by the methods, solid state ligand exchange and solution-phase ligand exchange. During the ligand exchange process long ligand molecules are changing with the short ones to reduce interparticle spacing and increase the conductivity.

Another critical parameter is the size of the QDs, since it determines the absorption spectrum of QDs. The size of the QDs varies with growth temperature and time. As

the size of the QD reduced, the absorption peak blueshifts (figure 2.8). On the contrary, with increasing the size of the QD absorption peak redshifts [22].

One of the most popular and widely used IR photodetector material is lead (II) sulfide (PbS) CQDs which operated in SWIR. It has wide tunable band gap from 0.6 eV to 1.6 eV, high Bohr exciton radii with ~18 nm, as well as significant stability in air. In addition, they have comparable photodetector performance with commercial materials. The advancement of ligand exchange technology allowed PbS QDs to have their carrier mobility, work function, and carrier concentration adjusted while maintaining their stability. Because of all mentioned properties of PbS QDs, they have an increasing demand and usage field in the IR region [26].

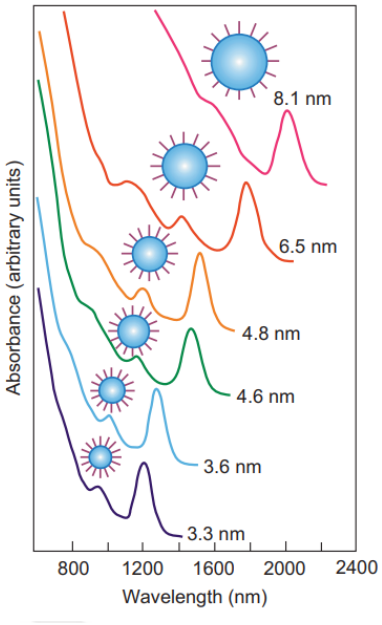

Figure 2. 8 Size depended absorption peaks of PbS QDs.

CHAPTER 3

EXPERIMENTAL STUDIES

This chapter focuses on first the experimental work for the transport layers and examines the effect of the transport layers on the device performance by using different characterization methods. Later on, to enhance an easy and cost-effective fabrication, several experimental studies on the thickness of the quantum dot absorber layer have done.

3.1 Device Description

In this work, a heterojunction photodiode fabrication was performed. Device structure and energy band alignment of the stack are shown in figure 3.1.

A junction was created between two QD layers treated with two different ligand molecules. One of the two ligand treatments produced a p-type layer, whereas the other one produced an n-type layer [27].

The structure of the device includes p and n-type QD absorber layers that were sandwiched between transport layers; electron transport layer (ETL) and hole transport layer (HTL). Electrode materials were placed on two opposite sides of the device.

A way to utilize thicker absorbers is to form a junction of two QD layers containing different ligands. A combination of a p-type with an n-type ligand can offer the necessary build-in field for the junction formation while simultaneously block the carrier flow towards in the opposite direction. Furthermore, employing two QD layers can significantly boost the stack absorption by giving possibility to use thicker absorber layer [28, 29].

As an electron transport layer (ETL), mostly wide-bandgap transparent metal oxides were used. This layer has n-type character and reduces the dark current by blocking holes come from the cathode side under reverse bias. Another transport layer in the structure that was used is named hole transport layer (HTL) blocks the injection of

electrons which come from the anode side (figure 3.1). As HTL wide band gap p-type materials were used. This HTL material was coated on the opposite side of the ETL. However, transport layers also help to create a suitable energy band alignment in the stack and prevent charge recombination. The thickness of the transport layers is important for the device efficiency. They must have an optimum thickness value, as very thick layers can cause a high resistivity.

For the charge collection, top and bottom contacts were placed on the two sides of the device. As an electrode, a transparent material was applied where the illumination comes from to let incoming light into the structure. However, for the electrode on the other side, a reflective material was applied to reflect back the photons that did not participate in the absorption in the first pass.

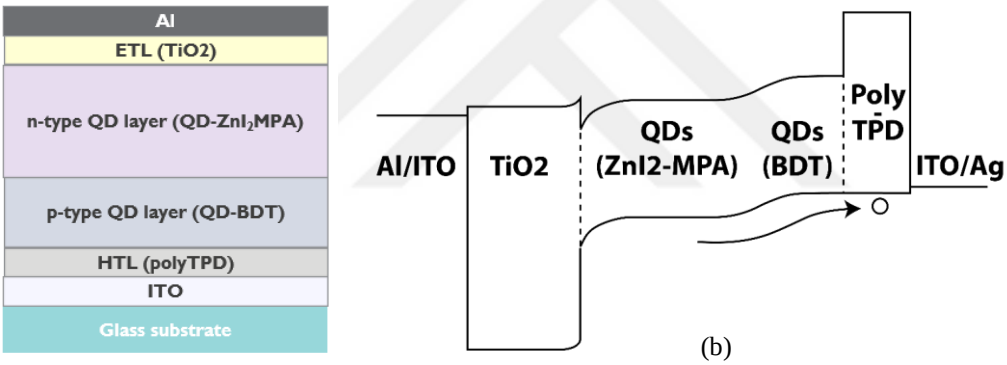

(a) (b)

Figure 3. 1 The structure (a) and energy band alignment of the device (b)

3.2 Device Fabrication

Several steps were taken to develop a photodetector structure that can be integrated on a readout integrated circuit (ROIC) based on complementary metal-oxide-semiconductor (CMOS) technology. In the first stage, a photodetector structure was developed on a glass substrate. Here the stack was examined electrically by bottom illumination. The processing was started with glass substrate to make the fabrication

more cost effectively. Then, the stack was integrated onto the silicon substrate to examine it under the illumination that comes from top contact side. These steps were followed to optimize the stack for CMOS ROIC integration (figure 3.2).

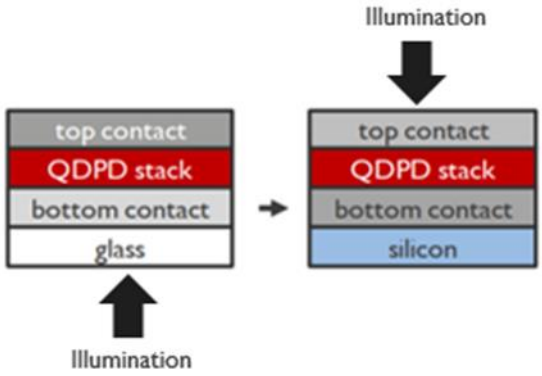

Figure 3. 2 Device optimization steps [6]

In this study, indium tin oxide (ITO) coated glass substrates were used due to the low resistivity and high transparency of the ITO material. The layout design of the glass pads has two ITO strips shown in the figure. The full stack of the photodetector was deposited on the glass/ITO. A specially designed mask was used during ETL application to prevent material from depositing to the edges. When the solid stack was deposited on the substrate, the end sides of the ITO strips were scratch manually to create the bottom contact points. Top contact deposition was occurred after the end sides of the ITO strips were properly cleaned. The typical design of the samples has 12 devices on (each for 0.13 cm^2 area) shown in figure 3.3.

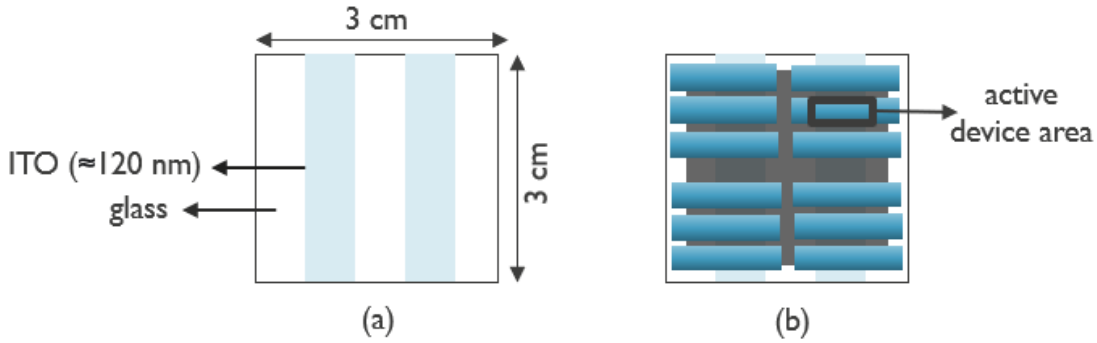

Figure 3. 3 Design of the ITO/glass substrate before (a) and after (b) full stack deposition

As the second stage, the fabrication of the devices was transferred to the silicon substrates that have as-prepared contact pads which mimic CMOS ROIC design (figure 3.4). In this study, silicon substrates that have contact pads (having 0.065 cm^2 area) made of copper (Cu) and titanium nitride (TiN) was used. The design of the stack adjusted for top illumination conditions in this step. As a top contact material, transparent ITO was used.

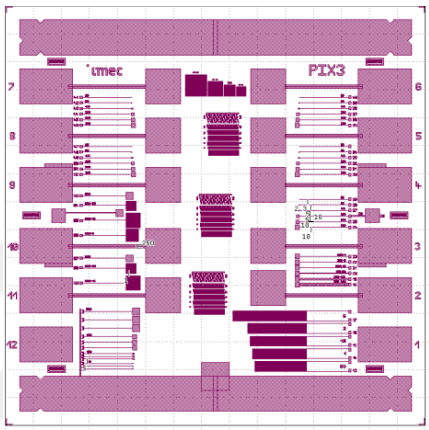

Figure 3. 4 Design of the silicon substrates [27]

Devices on a glass or silicon substrate should perform roughly the same from an electrical point of view, as they all have interfacing in the same order. Due to lighting from different directions, top and bottom, the optical properties might be different for the devices on silicon or glass substrates [30].

3.3 Fabrication Steps and Used Materials

3.3.1 Hole Transport Layer

Several materials were tasted in this study. HTL application of each different materials were done by spin coating technique from solutions. Organic polymer Poly(N,N'-bis-4-butylphenyl-N,N'-bisphenyl)benzidine (PolyTPD) (figure 3.5a) was the mainly used material as HTL. Devices with PolyTPD HTL were used as a reference sample. 2-(9H-Carbazol-9-yl) ethyl] phosphonic (2PACz) (figure 3.5b) and nickel oxide (NiO_x)

were tested as HTL, respectively. NiO_x sputtered substrates were used in this study. However, the other chemicals were obtained from commercial suppliers.

Once spin coating process was done for HTL, they were annealed at 80°C for 10 minutes on a hotplate placed in nitrogen filled glovebox.

NiO_x coated substrates were heated on a hotplate at 300°C for 30 minutes in ambient environment to reduce its metallic feature before the active layer deposition.

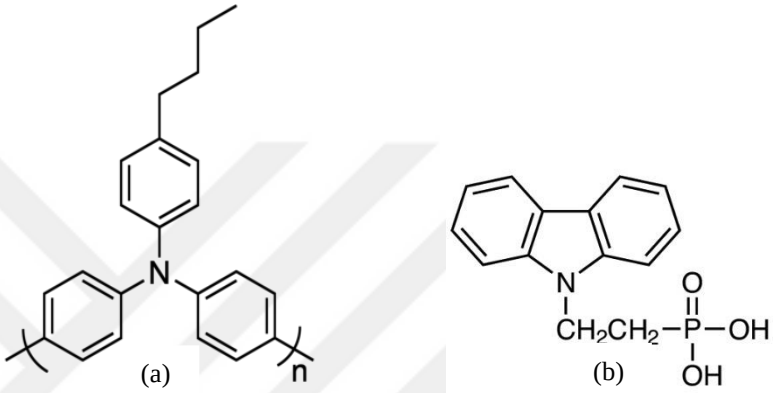

Figure 3. 5 Molecular structure of PolyTPD (a) and 2PACz (b)

3.3.2 Active Layer

Lead Sulfide (PbS) QDs, having long oleic acid ligand molecules dissolved in n-octane were applied as an active layer on the substrate with a spin coater. QD materials with a size of ~6.4 nm and an exciton absorption peak of 1550 nm were obtained from Quantum Solutions. The solid-state ligand exchange method was used to replace the long oleic acid ligands with shorter ligands. By doing so, the electrical properties of the films were improved. The desired thickness of the active layer was achieved by applying several thin layers to allow the ligand solution to penetrate the film and the ligand exchange process to occur properly.

Each layer consists of three steps: QD application, ligand solution application, and washing. The QD layer was covered with the ligand solution and left for a period of time to penetrate the film. Ligand exchange causes layer shrinkage due to the

displacement of long ligand and short ligand molecules. However, the defects formed during ligand exchange are filled by the other thin layer of QD. Then, the residues were removed by washing twice using the solvents of the ligand molecules.

3.3.3 Ligands

In this study, two different ligand types; organic 1,4 benzene dithiol (BDT) and zinc iodide with 3-mercaptopropionic acid (ZnI_2:MPA) were used. BDT dissolved in acetonitrile was applied to the QD film for the ligand exchange process insulating oleic acid ligand molecules with shorter BDT ligand molecules. Short thiol-based ligands have been extensively utilized in photodetector structures to create p-type CQD solids [31, 32, 33, 34]. For subsequent doping, QD-BDT-deposited substrates were left overnight in a dry oxygen cabinet.

However, for the n-type QD layer , ZnI_2:MPA dissolved in anhydrous ethanol was applied to the QD film. The mixed organic MPA and inorganic ZnI2 treatment have been used since it has reduced sub-bandgap traps and it results in good passivation [35].

Ligand materials were purchased from a chemical supplier.

3.3.4 Electron Transport Layer

In In the structure, various materials (generally wide band-gap metal oxides) were used to block the holes are generated in the active layer and allow the electrons to move to the cathode side. In this study, titanium dioxide (TiO_2) was used as the ETL material. Devices with TiO_2 ETL were used as a reference sample. Then, magnesium doped zinc oxide (ZnO:Mg), buckminsterfullerene (C_{60}) (figure 3.6a), buckminsterfullerene (C_{60})/bathocuproine (BCP) (figure 3.6b) were tested, respectively.

Different deposition techniques were applied to various materials. TiO_2 is most widely used ETL material in this study, was deposited by electron beam deposition technique (one of the physical vapor depositions (PVD) techniques) at a speed of 0.5 Å/s and a thickness of 20 nm. C_{60} and BCP were deposited by using the thermal evaporator at

40 nm and 5 nm thickness, respectively. Finally, spin coating deposition technique was used to deposit ZnO:Mg.

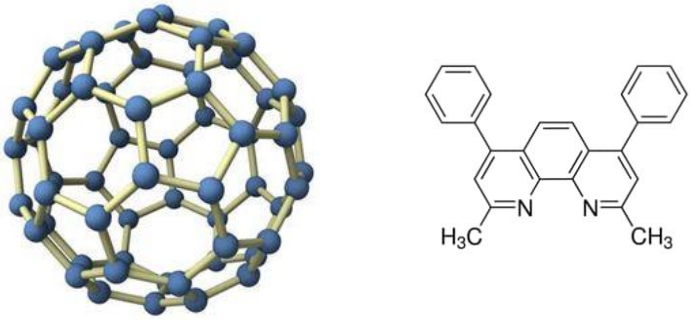

Figure 3. 6 Molecular structure of C_{60} (a) and BCP (b)

Solution-based applications are cost-effective compared to PVD methods that require a vacuum environment. However, PVD methods are more accurate for giving the possibility to adjust the thickness.

3.3.5 Contacts

In this study, different contact materials were used depending on the type of substrate, glass or silicon.

Glass surfaces with pre-patterned ITO were used as bottom contacts. Furthermore, aluminum (Al) reflective top contacts were deposited on glass substrates with a thickness of 120 nm and a speed of 1 Å/s by a thermal evaporator. Prior to insertion of the top contact, all other layers on the samples were scratched from the edges of the ITO strips to be able to probe the device.

For the silicon substrate, the design of the device is adjusted due to the top illumination. The silicon substrate has an architecture with bottom metal contacts that mimics the CMOS ROIC design. Titanium Nitride (TiN) which is typical material for CMOS flow and copper (Cu) were the materials used as bottom contacts in this study. ransparent ITO (100 nm) was used as the top contact for devices on a silicon substrate.

CHAPTER 4

CHARACTERIZATION METHODS

The optical and electrical properties of the devices were examined in this part of the study. Dark current under reverse bias voltage and EQE measurements were the essential interest points for the device optimization.

4.1 Current-Voltage Measurement

The four-probe technique with the voltage range -3V to 3V and the step of 0.01V was applied under dark conditions. Even though the forward current also gave us information about the device, the main focus of interest was the reverse dark current. In order to compare the devices with different active device areas, the current values obtained were divided by the active device area and, the current density (J) values were obtained.

4.2 External Quantum Efficiency

Considering the detection range of the used absorber QD material, mainly the range of 1100-1700 nm was used during EQE vs. wavelength measurement with a measuring step of 10 nm by exposing the device to monochromatic light. Followingly, EQE vs. voltage measurement was done at the peak wavelength (generally 1550 nm) from 0V to -3V with a step of 0.1 V. All the measurements were done in an environment which is isolated from the ambient light. A germanium cell was used for the setup calibration before starting to the measurements.

Reflection and transmission measurements were also recorded by using the same setup.

CHAPTER 5

RESULTS AND DISCUSSION

The focus of this chapter is to discuss the obtained results after certain number of experiments that were done with the aim of the device performance optimization.

This chapter comprises two parts. One is the investigation of new HTLs and ETLs by using glass substrates to improve device performance. Then with the best performing transport layers, we designed a new concept which involves less QD absorber layers and an antireflection layer.

5.1 ETL Studies

In this section various wide band gap metal-oxides and organic materials were used as electron transport layer (ETL) via different deposition methods. ETL has a significant effect not only on hole blocking and extracting of electrons, but also on carrier transport speed and device efficiency in optoelectronic devices [36]. Therefore, to suppress the dark current, it is important to choose the right material that can form a perfect junction with the QD surface and has energy levels compatible with the active layer.

During the experiments, the full device was kept the same except ETL. However, deposition was performed in an inert environment for all devices.

Firslty, ZnO:Mg was tested in the structure of the device. We used ZnO doped with Mg because, by increasing Mg content in ZnO, its conduction band minimum (CBM) level become closer to the vacuum level. This may result in a reduced electron injection barrier at the interface of the ETL and QD active layers via CBM upshifting [37].

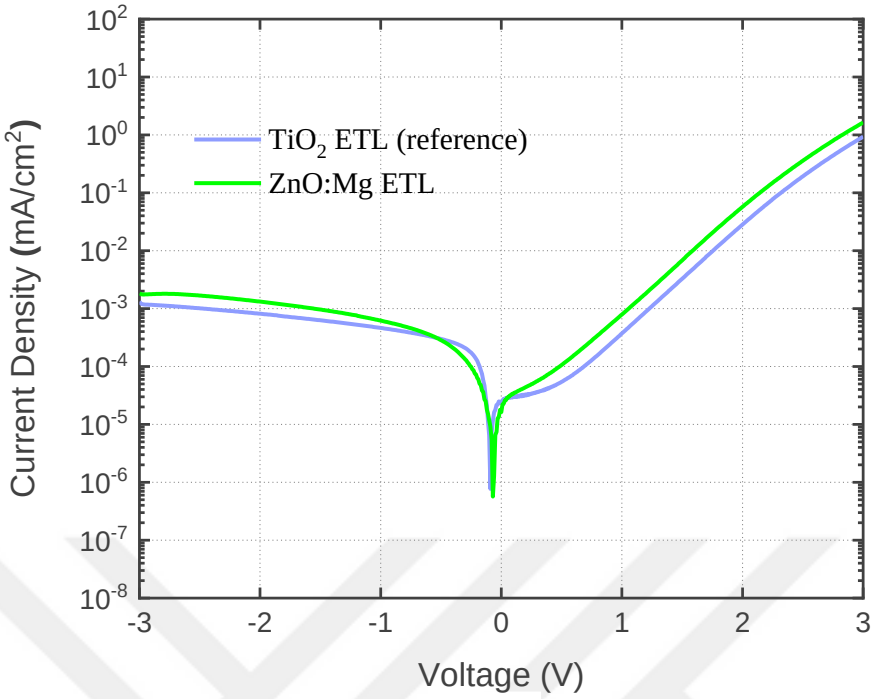
Current Density (mA/cm^2)
10^2
10^1
10^0
10^{-1}
10^{-2}
10^{-3}
10^{-4}
10^{-5}
10^{-6}
10^{-7}
10^{-8}
TiO$_2$ ETL (reference)
ZnO:Mg ETL
-3
-2
-1
0
1
2
3
Voltage (V)

(a)

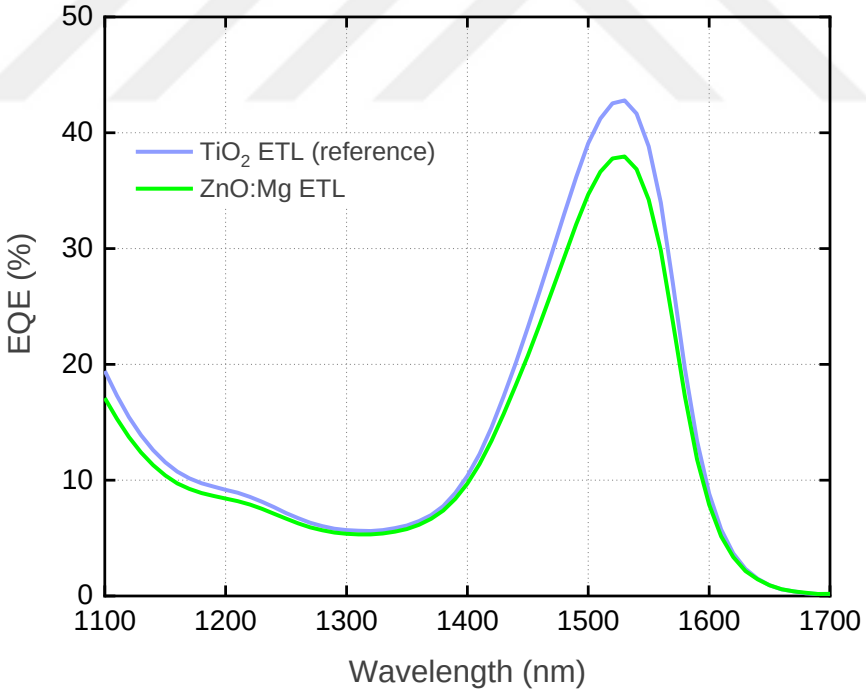
EQE (%)
50
40
30
20
10
0
TiO$_2$ ETL (reference)
ZnO:Mg ETL
1100
1200
1300
1400
1500
1600
1700
Wavelength (nm)

(b)

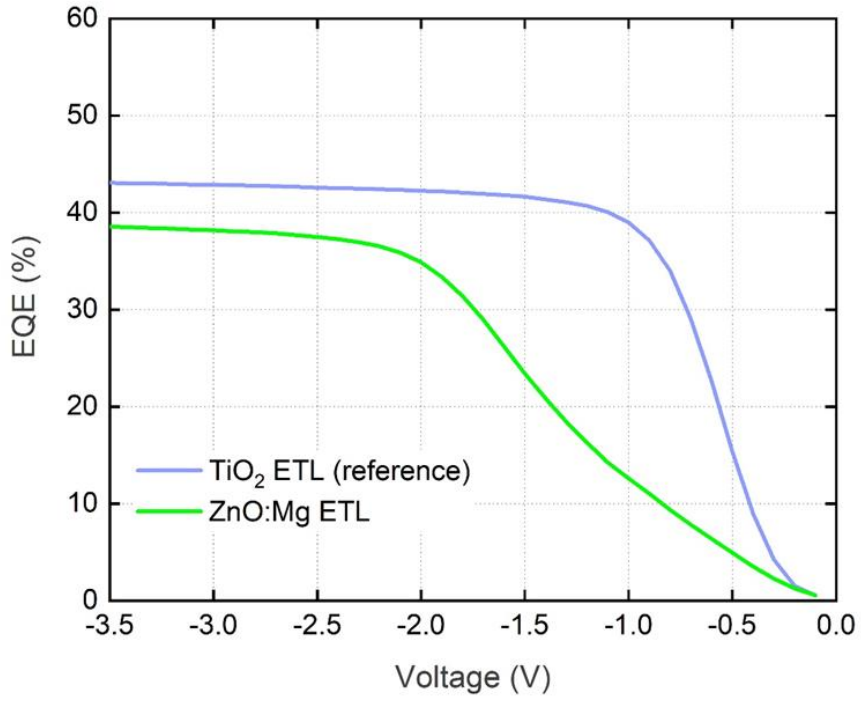

(c)

Figure 5. 1 JV (a), EQE-Wavelength (b) and EQE-Voltage (c) curves for performance comparison of the devices with TiO_2 ETL and ZnO:Mg ETL

TiO_2 as a well-known, and the most commonly used material was used in the structure of the control sample. Figure 5.1 shows EQE and JV curves of the experiments with ZnO:Mg ETL. TiO_2 was used for comparison as a reference sample. ZnO is a material that has electron mobility several orders of magnitude higher than TiO_2 [36]. In this study, the device with TiO_2 ETL shows slightly lower dark current and higher EQE values as shown in figure 5.1a and figure 5.1b, respectively. However, EQE -voltage plot demonstrates that the device which has ZnO:Mg ETL is more resistive than the reference sample as it needs higher voltage values to reach its maximum EQE value (figure 5.1c). Therefore, the reference sample shows better performance compared to the device with ZnO: Mg ETL. This can be attributed to a bad contact between QD-ETL interfaces.

It is known that UV light has an effect on ZnO conductivity. ZnO contains chemisorbed non-lattice oxygen on its surface that extracts free electrons of ZnO. This reduces the conductivity of ZnO. However, after a certain period of exposure to UV light, photoexcited holes are formed which might capture electrons from the surface of chemisorbed oxygen then become discharged and free from the surface [38]. For this reason, samples containing ZnO:Mg ETL were exposed to UV light. The difference between before and after UV exposure of ZnO shown in the figure 5.2. The EQE of the device increases as a result of UV exposure (figure 5.2a). In addition, the EQE-Voltage graph shows that conductivity of the device is also increased since it needs less voltage to reach to its maximum EQE value (figure 5.2b). ZnO has better performance after compared before UV exposure.

Due to its high electron extraction ability, the second material tested was Buckminsterfullerene (C_{60}), an organic fullerene. This material was deposited at thickness of 40 nm with a thermal evaporator. Since C_{60} is an oxygen-sensitive

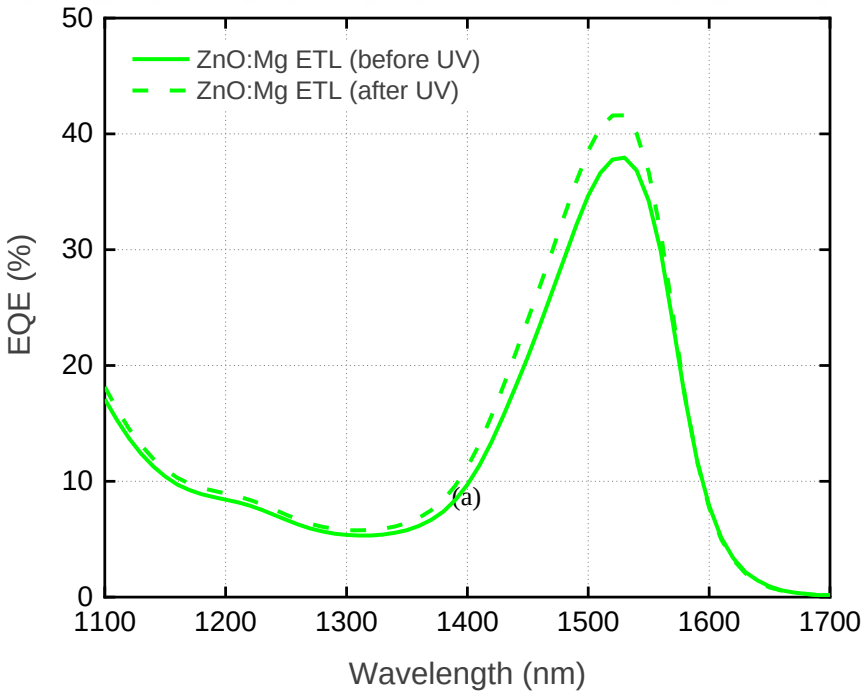

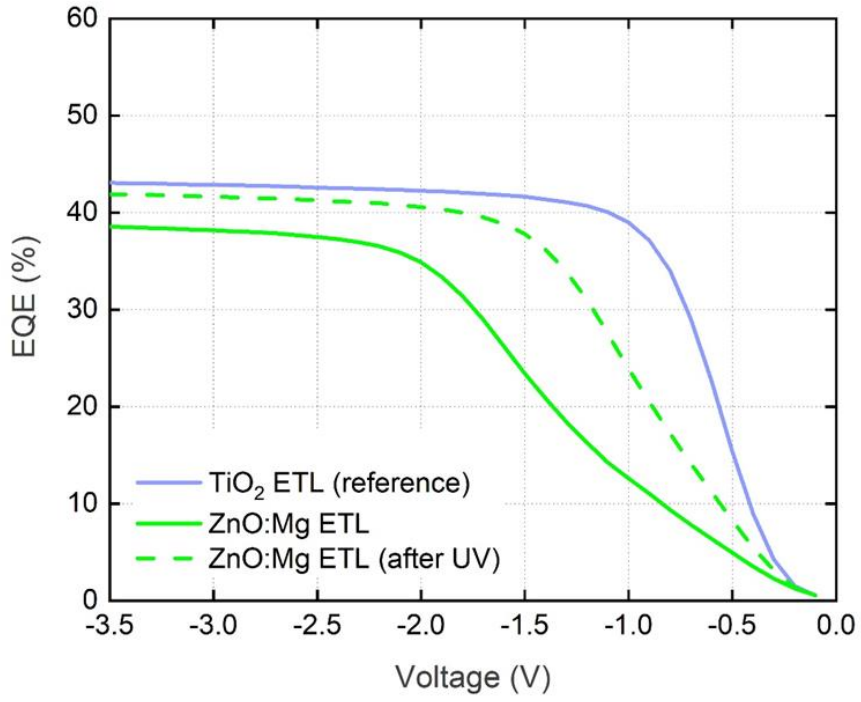

(b)

Figure 5. 2 EQE-Wavelength (a) and EQE-Voltage (b) curves shows performance improvement after UV exposure

material, the deposition was carried out in an oxygen-free, inert environment. Likewise, device characterization was performed in an oxygen-free environment.

Figure 5.3 shows IV and EQE plots for the device with C_{60} ETL and reference sample. The dark current of the device with C_{60} is lower than the reference sample (figure 5.3a). However, there is also a decrement in forward current. That indicates that the device with C_{60} ETL is more resistive than the reference sample. This situation is also proven with a lower EQE (figure 5.3b). Furthermore, in EQE-Voltage graph, it observable that the device with C_{60} needs higher voltage values than the reference to reach to the maximum EQE of the device.

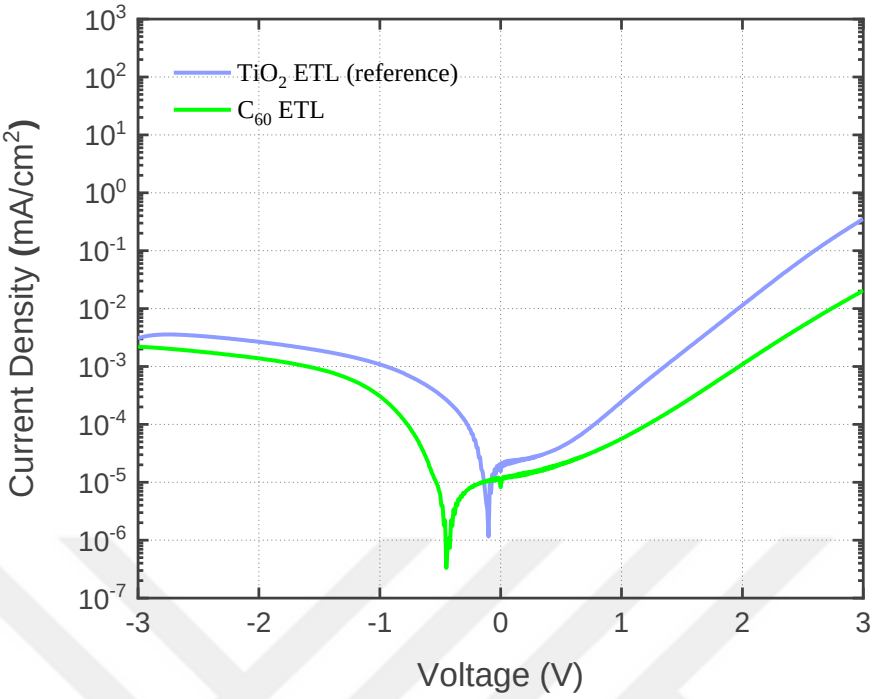
TiO2 ETL (reference)
C60 ETL
Current Density (mA/cm2)
Voltage (V)

(a)

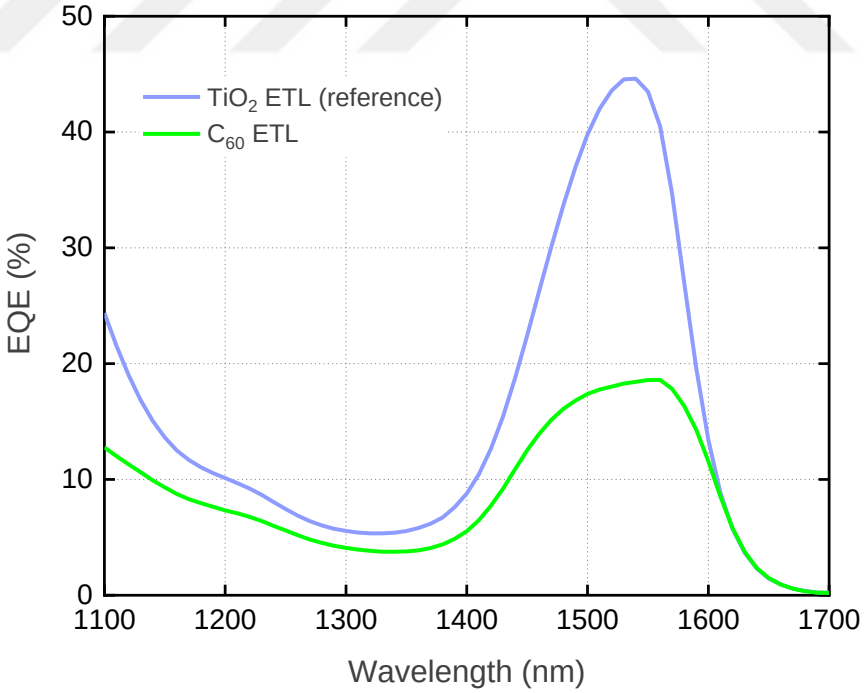
TiO2 ETL (reference)
C60 ETL
EQE (%)
Wavelength (nm)

(b)

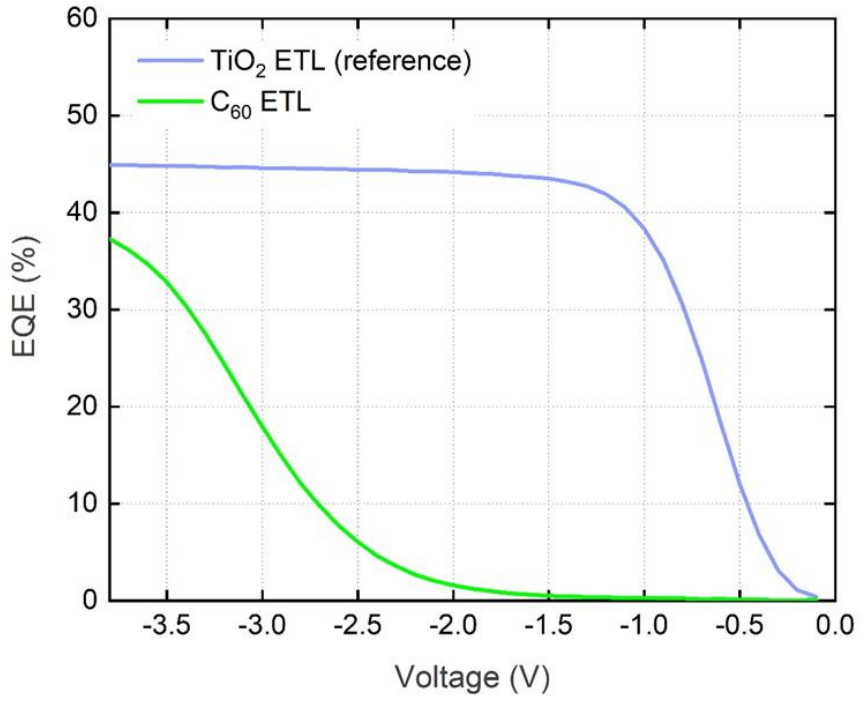

(c)

Figure 5. 3 JV (a), EQE-Wavelength (b) and EQE-Voltage (c) curves for performance comparison of the devices with TiO_2 ETL and C_{60} ETL

To investigate the cause of the device resistance issue, we reduced the thickness of the C_{60} from 40 nm to 20 nm. Figure 5.4 shows how the EQE and IV values change with decreasing thickness. In the I-V graph, there is an observable change in forward current with varying thickness (figure 5.4a). Furthermore, as the thickness of the C_{60} decreases, the EQE increases (figure 5.4b). Higher forward current and higher EQE indicate that devices with thicker C_{60} ETL have higher resistance. However, the EQE-Voltage graph shows that it still needs higher voltage values than the reference sample to reach the maximum EQE (figure 5.4c). This indicates that the device still has high resistance.

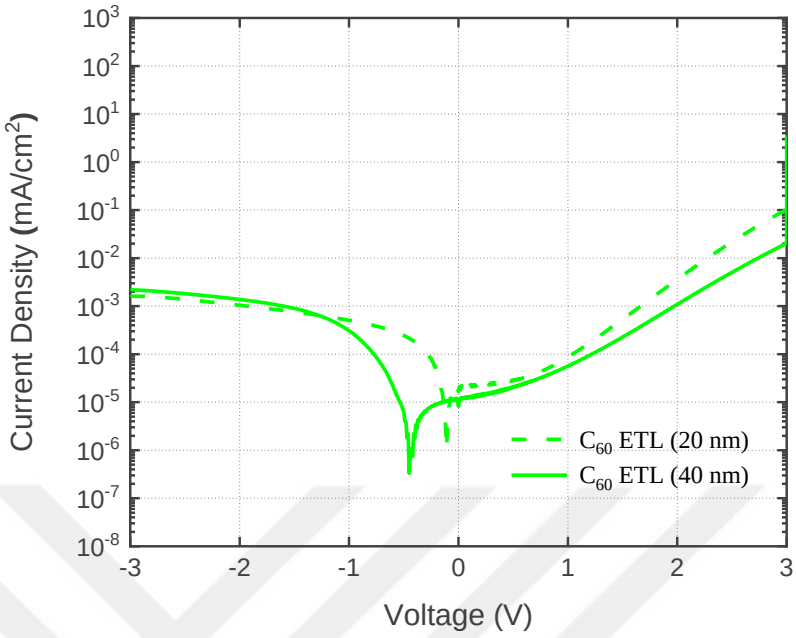
Current Density (mA/cm^2)
Voltage (V)
C_{60} ETL (20 nm)
C_{60} ETL (40 nm)

(a)

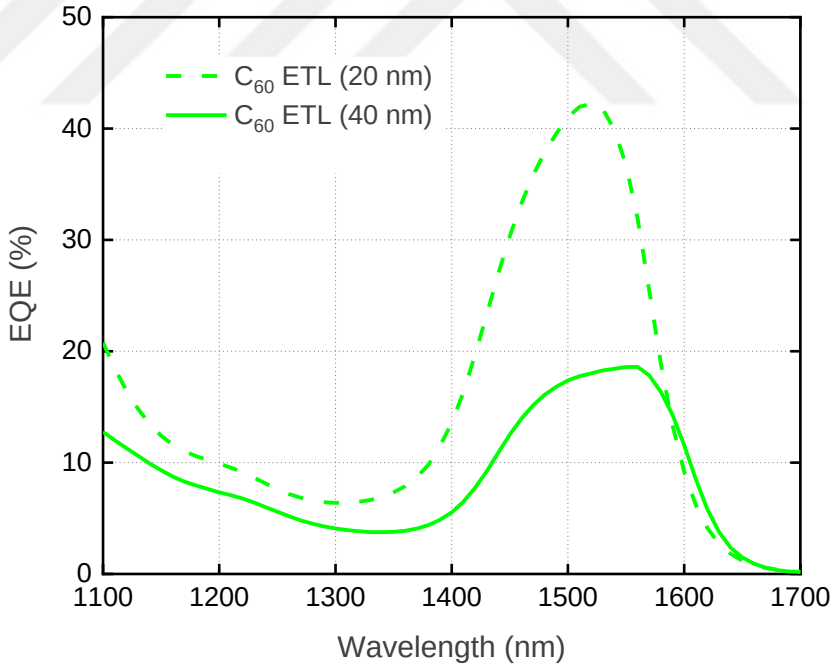
EQE (%)
Wavelength (nm)
C_{60} ETL (20 nm)
C_{60} ETL (40 nm)

(b)

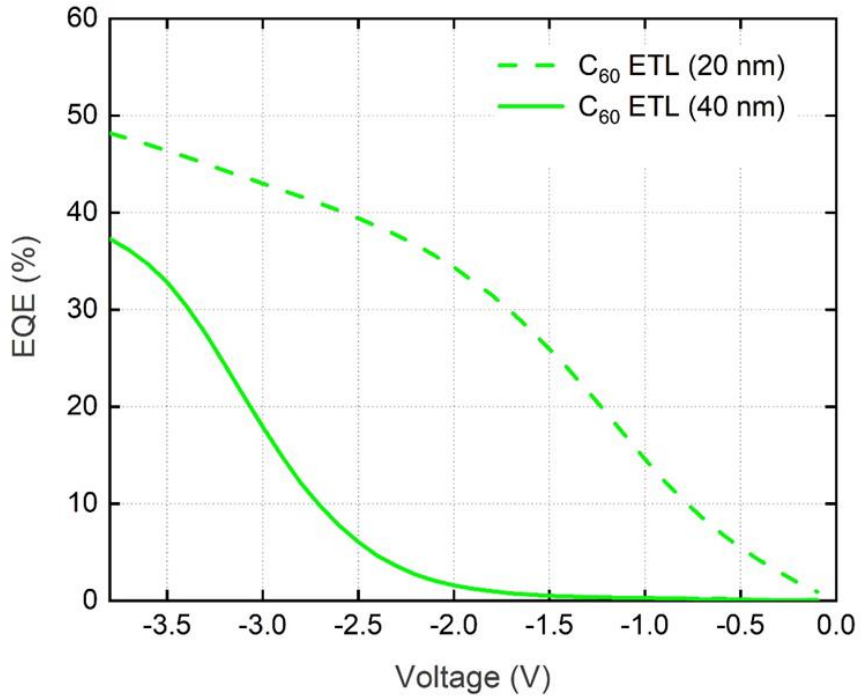

(c)

Figure 5. 4 JV (a), EQE-Wavelength (b) and EQE-Voltage (c) curves for the device with C_{60} ETL in different thicknesses

After some research, it has been observed that C_{60} may not form a uniform morphology and may contain defects that inhibit electron transport. In this context, we used BCP

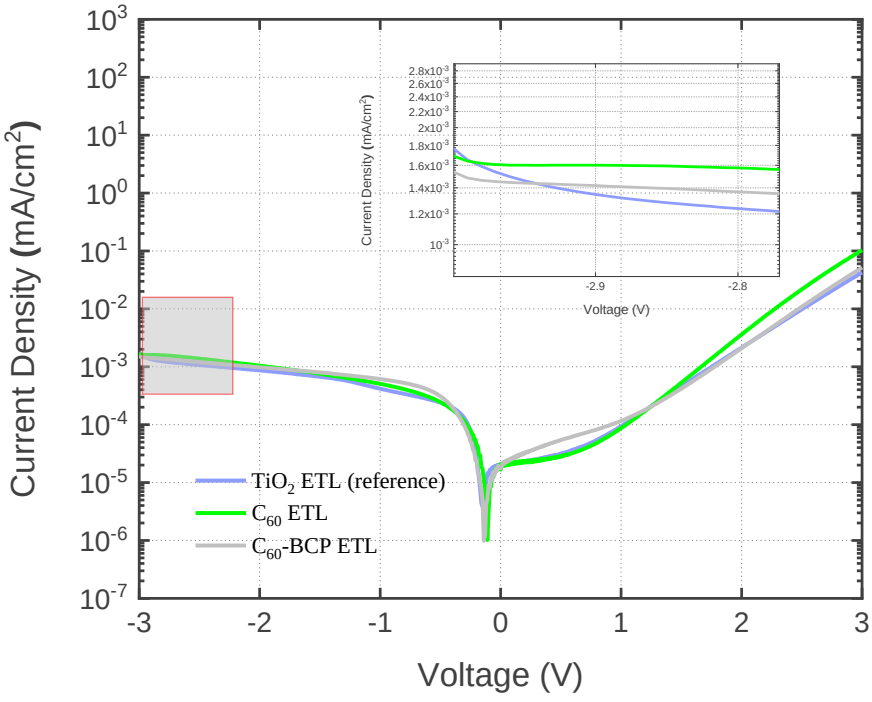

(a)

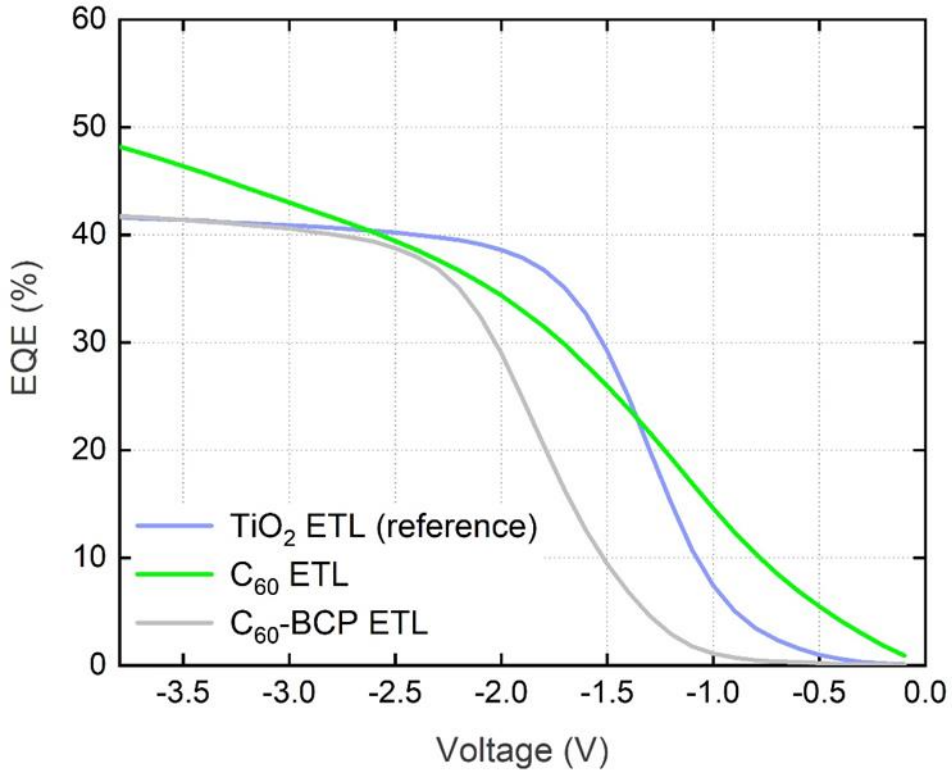

(b)

Figure 5. 5 JV (a), and EQE-Voltage (b) curves for the device with C_{60} ETL and the device with C_{60}-BCP ETL. It shows performance improvement after BCP application.

as a buffer layer in the photodetector structure for the first time in the literature to passivate the defects on the C_{60} surface and provide a smooth interface between C_{60} and the electrodes. As a result, there was an improved the electron transfer. A thin layer of BCP (5 nm) was deposited by a thermal evaporator in an inert environment.

As a result of this experiment, slight dropping in dark current was observed after BCP application (figure 5.5a). For the one with the BCP buffer layer shows slightly lower EQE than the one without BCP. However, EQE-Voltage plot indicates that the one with BCP buffer layer has less resistance than the one without BCP (figure 5.5b).

5.2 HTL Studies

After examining the effect of different ETLs, various materials were investigated to be used as HTL on the device with the best performing ETL.

First, NiO_x was tested on the same batch as an HTL material. NiOx as a HTL material is intensively researched because of their deep valance band edge, large bandgap, good thermal and chemical stabilities [39]. NiOx is a p-type semiconductor that can block electrons and transport holes [32].

NiO_x sputtered substrates were placed directly on a hot plate in ambient environment and heated at 300°C for 30 minutes to oxidize. This process was done to reduce the metallic features of the NiO_x layer. The sample with the PolyTPD layer as the HTL was used as the reference sample. As seen in Figure 5.6a, the higher forward current of the device with NiO_x HTL relative to the reference sample indicates that NiO_x has less resistance than PolyTPD. Also, NiO_x shows higher EQE (figure 5.6b). However, as the conductivity increases, there is an increment in the dark current.

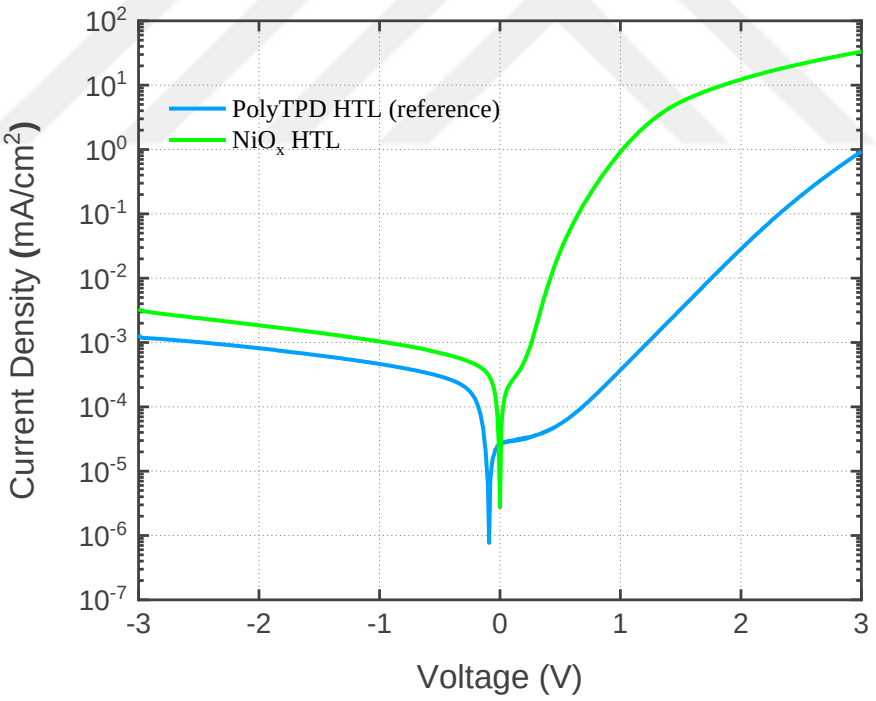

(a)

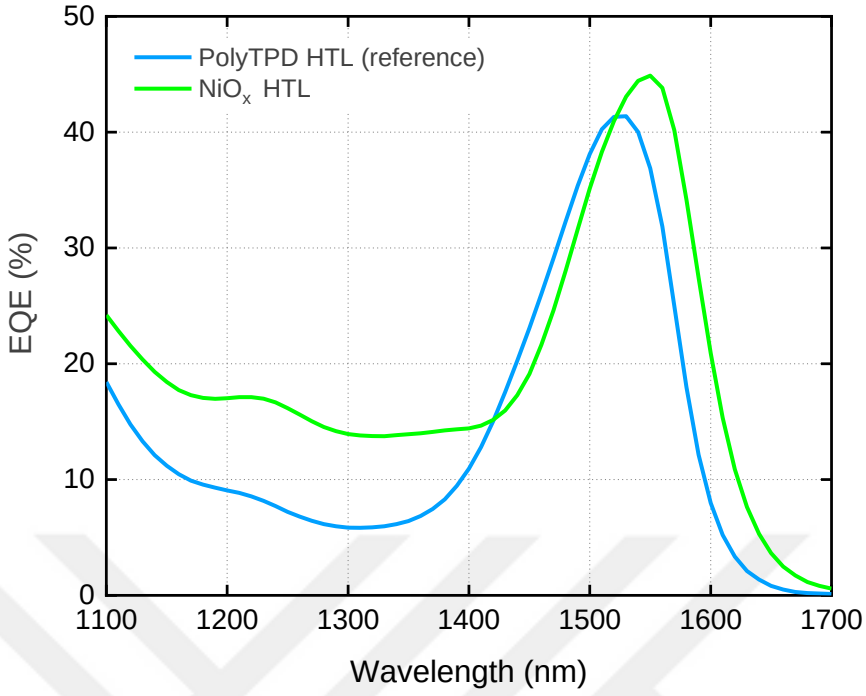

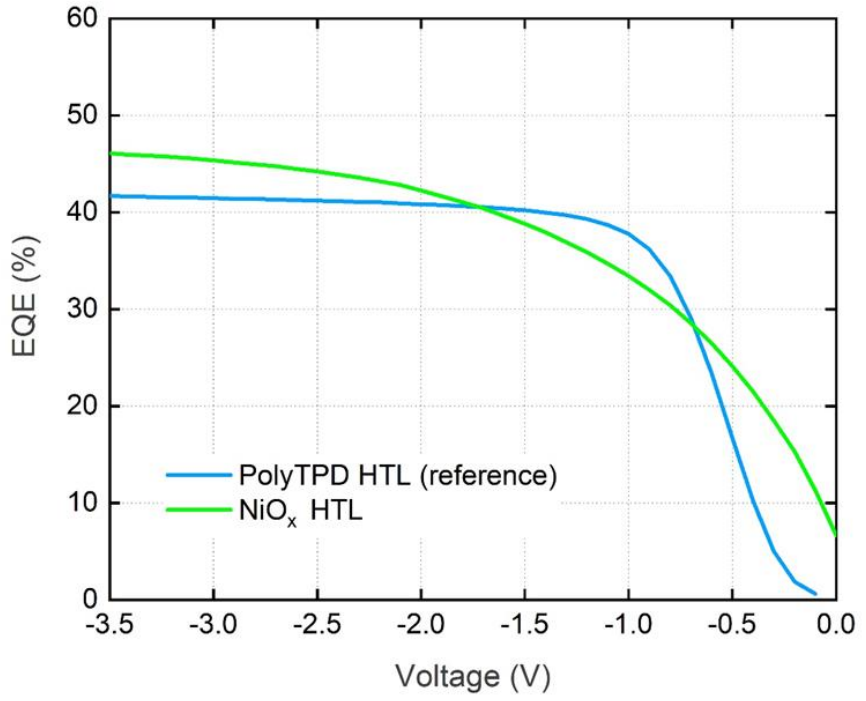

(c)

Figure 5. 6 JV (a), EQE-Wavelength (b) and EQE-Voltage (c) curves for performance comparison of the devices with PolyTPD HTL and NiO_x HTL

2PACz was tested as an HTL in the photodetector structure due to its certain number of advantages over PolyTPD. First of all, 2PACz is a self-assembled monolayer (SAM) that creates uniform and densely packed layers which may lead to an improvement in the hole transport [40, 41]. Moreover, as 2PACz contains the phosphonic acid anchoring group, it passivates interfaces, reduces defect density, and acts as a ligand for the QD-BDT layer. Phosphonic acid is also known for its ability to make strong bonds with metal ions and with ITO [42, 43]. Figure 5.7a shows JV curves measured for devices with PolyTPD and 2PACz HTLs. The higher forward current of the device with 2PACz than the device with PolyTPD can be clearly observed. This means that 2PACz has lower resistivity. High forward current of 2PACz is comparable with NiO_x. However, close dark current values were obtained from NiO_x HTL (figure 5.7b).

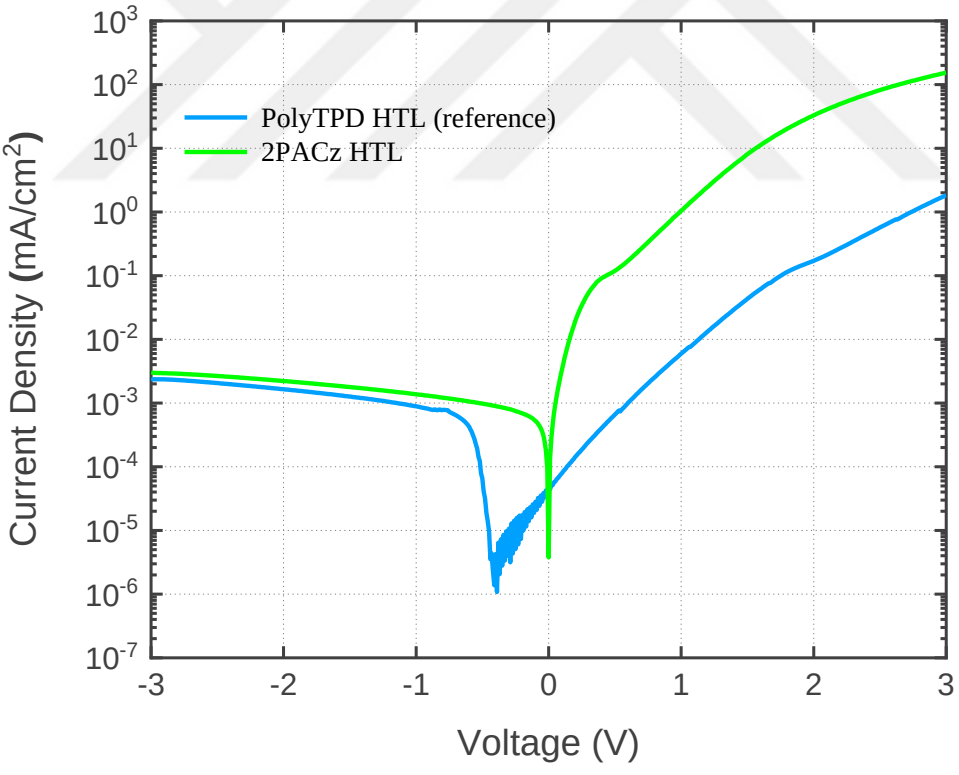

(a)

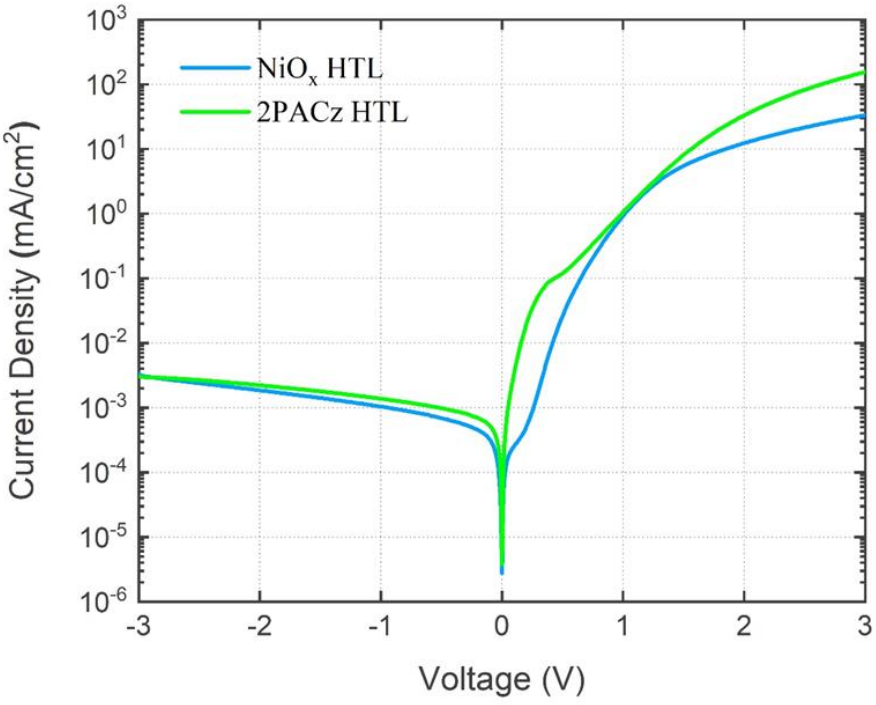

(b)

Figure 5. 7 JV curves for performance comparison of the devices with PolyTPD HTL and 2PACz (a), 2PACz HTL and NiO_x HTL (b)

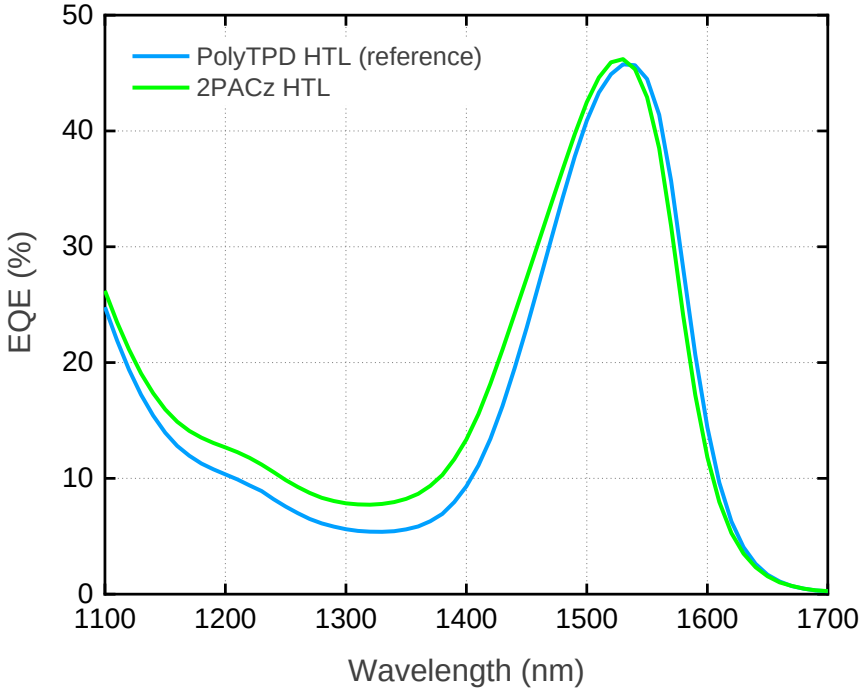

(a)

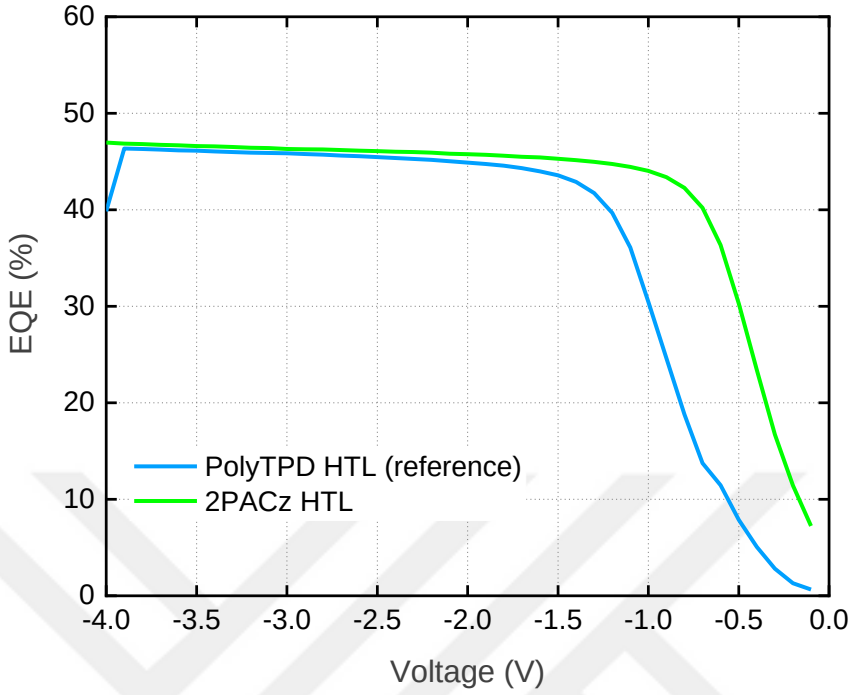

(b)

Figure 5. 8 EQE-Wavelength (a) and EQE-Voltage (b) curves for performance comparison of the devices with PolyTPD HTL and 2PACz HTL

2PACz and PolyTPD show almost the same EQE values at around 1550 nm (Figure 5.8a). However, as figure 5.8b shows, the device with 2PACz HTL needs less reverse voltage value to reach maximum EQE.

5.3 Thinner Absorber Layers Compensated with an Antireflection Layer

Easy and cost-effective manufacture of devices for mass production is always important. Since it takes time to bring the QD layers to the optimum thickness value, several research and work has been done in this section to solve this problem.

In the standard structure produced by our research group, there are 12 layers of QD that have ZnI_2:MPA ligand molecules (n-type) and 4 layers of QD that have BDT ligand molecules (p-type). The concentration of the quantum dot solution is 40 mg/ml (figure 5.9). However, the large number of layers makes the production process more difficult and expensive. Therefore, it is necessary to reduce the thickness of the QD

layers. However, as the thickness of the absorber layer decreases, the EQE will directly decrease due to less absorption. This situation makes the light utilization an important issue.

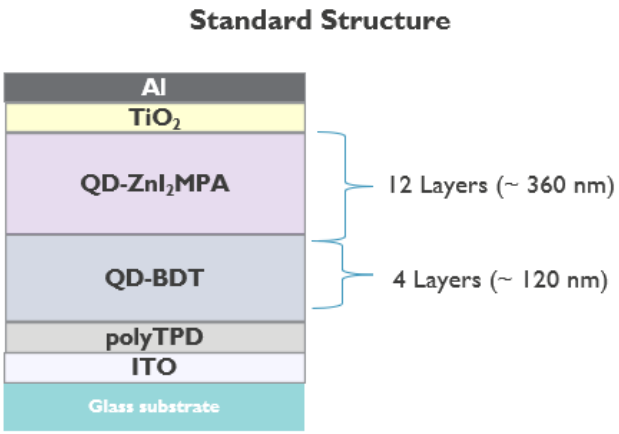

Figure 5. 9 Standart structure of the device that is developed by our research group.

As a way to compensate for the EQE value, we designed a stack with an anti-reflective layer on it. If the thickness of the layers is equal to the wavelength, the reflection of light back and forth between the interfaces of the layer becomes significant. In order to obtain a more accurate light distribution, it is necessary to include these effects by fine-tuning the thickness [44].

By using the anti-reflective layer, we have taken steps towards creating a constructive optical interference via adjusting the total thickness to maximize absorption. We used a transfer matrix method to simulate and extracted optical constants (n and k values) via ellipsometry measurements and fitting. The propagation of light into each layer of the stack was studied using the transfer matrix method [45].

5.4 Optimization of Thinner Absorber Layers

In this section, an attempt was made to reduce the thickness of the active layer by placing a lower concentration of the quantum dot solution and less layers. First, the

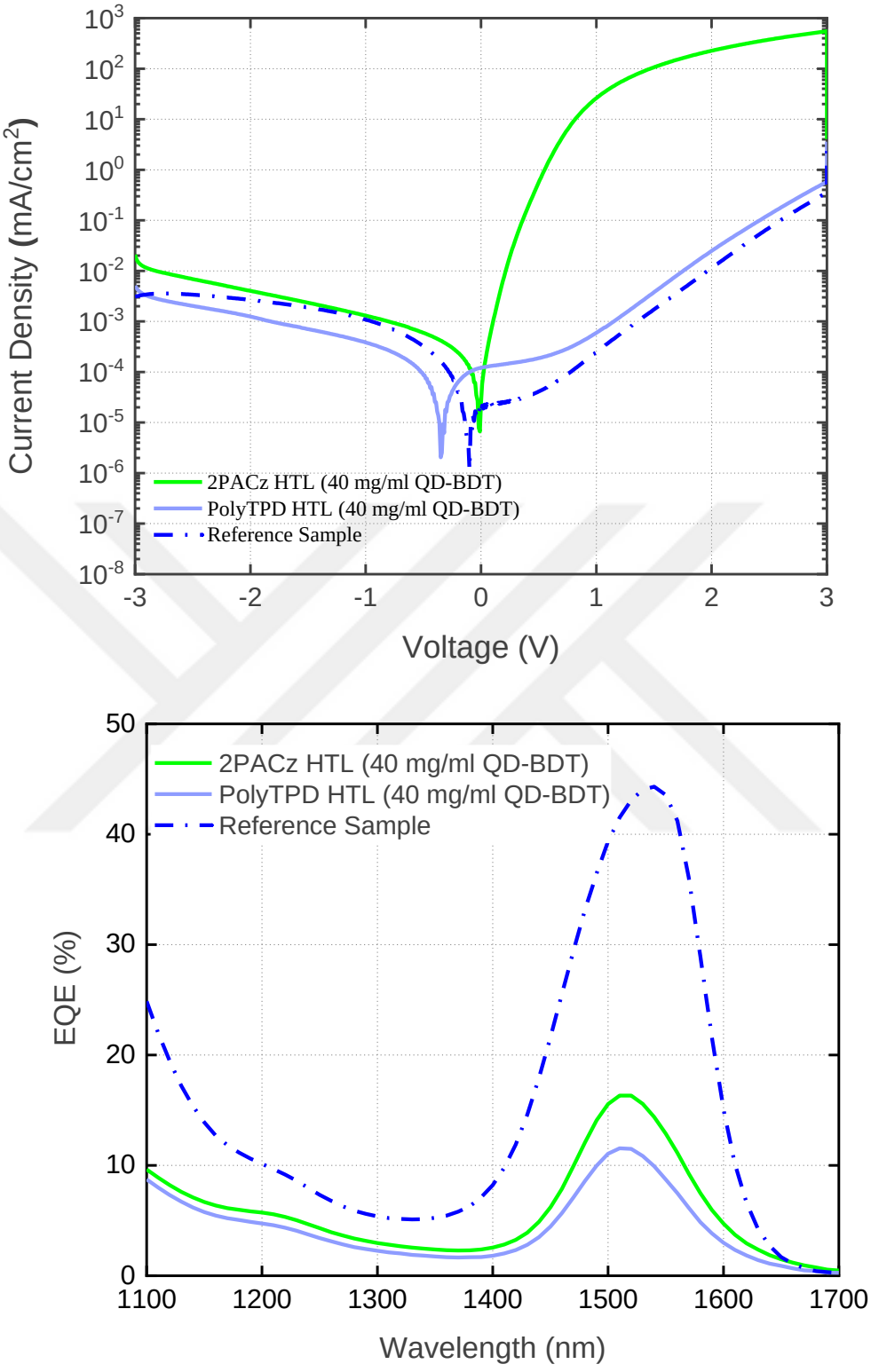

Figure 5. 10 JV (a) EQE-Wavelength (b) curves comparison for the devices with thinner absorber layers (containing 2 layers of QD-BDT and 6 layers of QD-ZnI_2:MPA, 40 mg/ml QD of solution concentration) and different HTLs

number of QD-BDT and QD-ZnI_2:MPA layers was halved by keeping the concentration constant at 40 mg/ml.

The best performing HTLs (2PACz and PolyTPD) and ETLs (TiO_2) were used at this stage due to the studies were carried out in the optimization of transport layers.

Figure 5.10a shows the JV curves of samples containing 2 layers of QD-BDT and 6 layers of QD-ZnI_2:MPA containing 40 mg/ml QD solution with different HTLs and their difference from the reference sample. The sample with the PolyTPD HTL shows almost the same dark current value as the reference sample at -3V.

In the EQE-Wavelength plot, shown in figure 5.10b, as expected, there was a decrement in EQE values after thinner active layer deposition. Due to the less resistivity of 2PACz, it has a higher EQE.

Second, the concentration of the QD-BDT layer was reduced to 20 mg/ml and the number of layers was kept the same as in the first step (2 layers QD-BDT, 6 layers ZNI_2:MPA). Here we reduced the concentration instead of reducing the number of layers. Because the cracks formed during ligand exchange owing to film volume loss are filled with the superposition of the other layer. Therefore, there must be at least two layers. Moreover, the QD concentration of the n-type QD layer remained constant at 40 mg/ml.

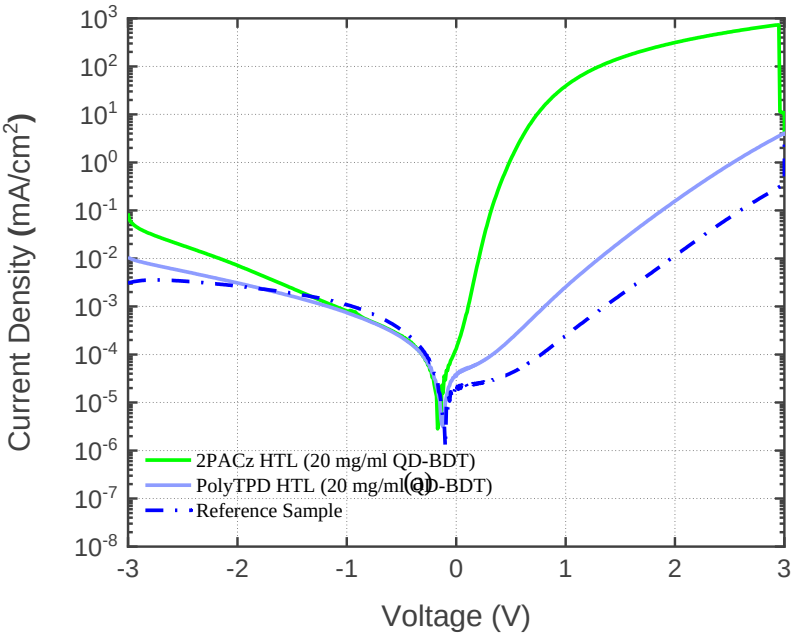

(a)

(b)

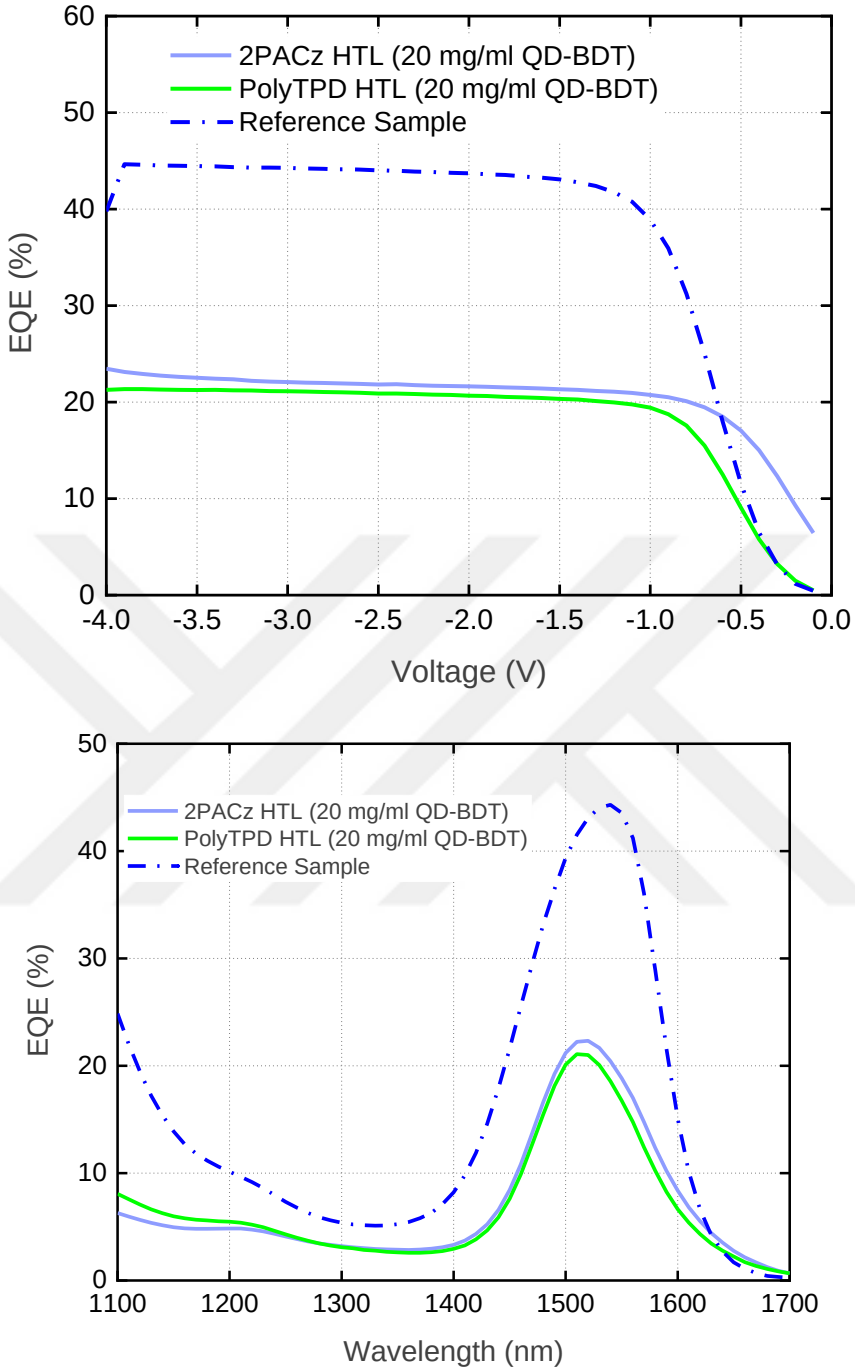

Figure 5. 11 JV (a) EQE-Wavelength (b) and EQE-Voltage (c) curves comparison for the devices with thinner absorber layers (containing 2 layers of QD-BDT and 6 layers of QD-ZnI_2:MPA, 20 mg/ml QD of solution concentration) and different HTLs

As shown in the figure 5.11a the sample with PolyTPD HTL has lower dark current than the sample with 2PACz, but higher dark current than the reference sample at -3V.

However, the EQE values of each sample increased after the concentration of the QD solution was reduced from 40 mg/ml to 20 mg/ml for the QD-BDT layer (figure 5.11b).

Figure 5.12 shows absorption values for the devices. Samples with a QD concentration of 20 mg/ml exhibited the highest absorption values.

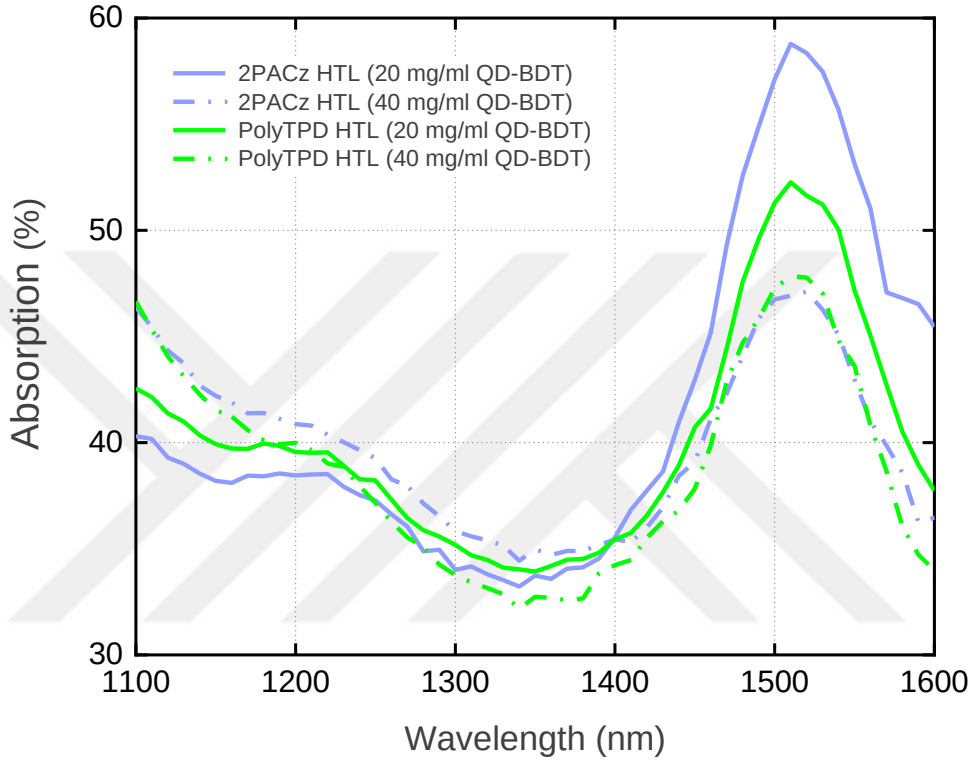

Figure 5. 12 Absorption curves of the devices with thinner layers and with different HTLs

5.5 Processing on Silicon Substrates and Antireflection Layer Coating

5.5.1 Processing on Silicon Substrates

Besides the studies of the device optimization on glass substrates, in this section optimization on silicon substrates of the best performing stacks was done. As already described in chapter 3, the stack was adjusted due to the top illumination conditions in this stage (figure 5.13).

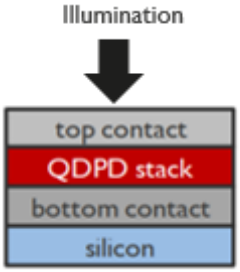

Figure 5. 13 Device design on silicon substrate

Best performing devices with thin absorber layers were transferred to silicon substrates that have bottom contact (TiN, Cu) mimicking the CMOS ROIC structure.

Firstly, as shown in the figure 5.14, we have tested different thicknesses for n-type ZnI_2:MPA layer by changing the number of layers; 6, 4 and 3.

The results of this study are shown in figure 5.15. In JV graph, it is observable that all the samples show lower forward current values than the devices on the glass substrate

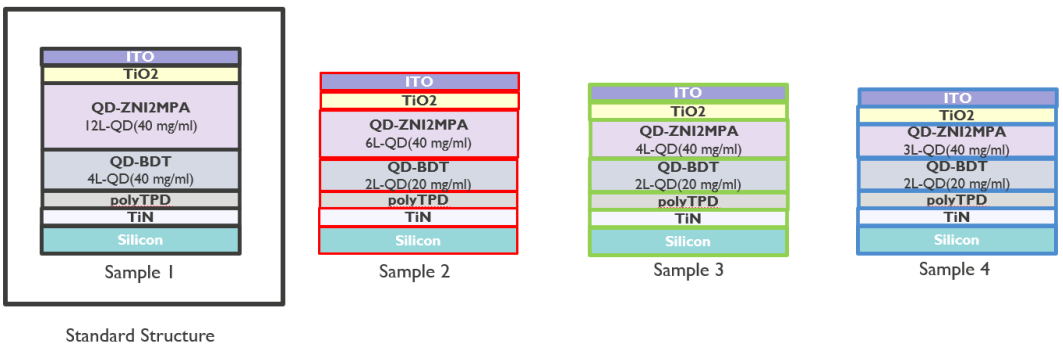

Figure 5. 14 Device structures with thinner absorber layers

(figure 5.15a). This is due to the high energy barrier of TiN in the stack band alignment. A high energy barrier hinders carriers jump over and participating in the current. However, dark current decreases with decreasing the thickness of the QD-ZnI_2:MPA layer. As expected, EQE values of the devices increase with an increasing thickness (figure 5.15b).

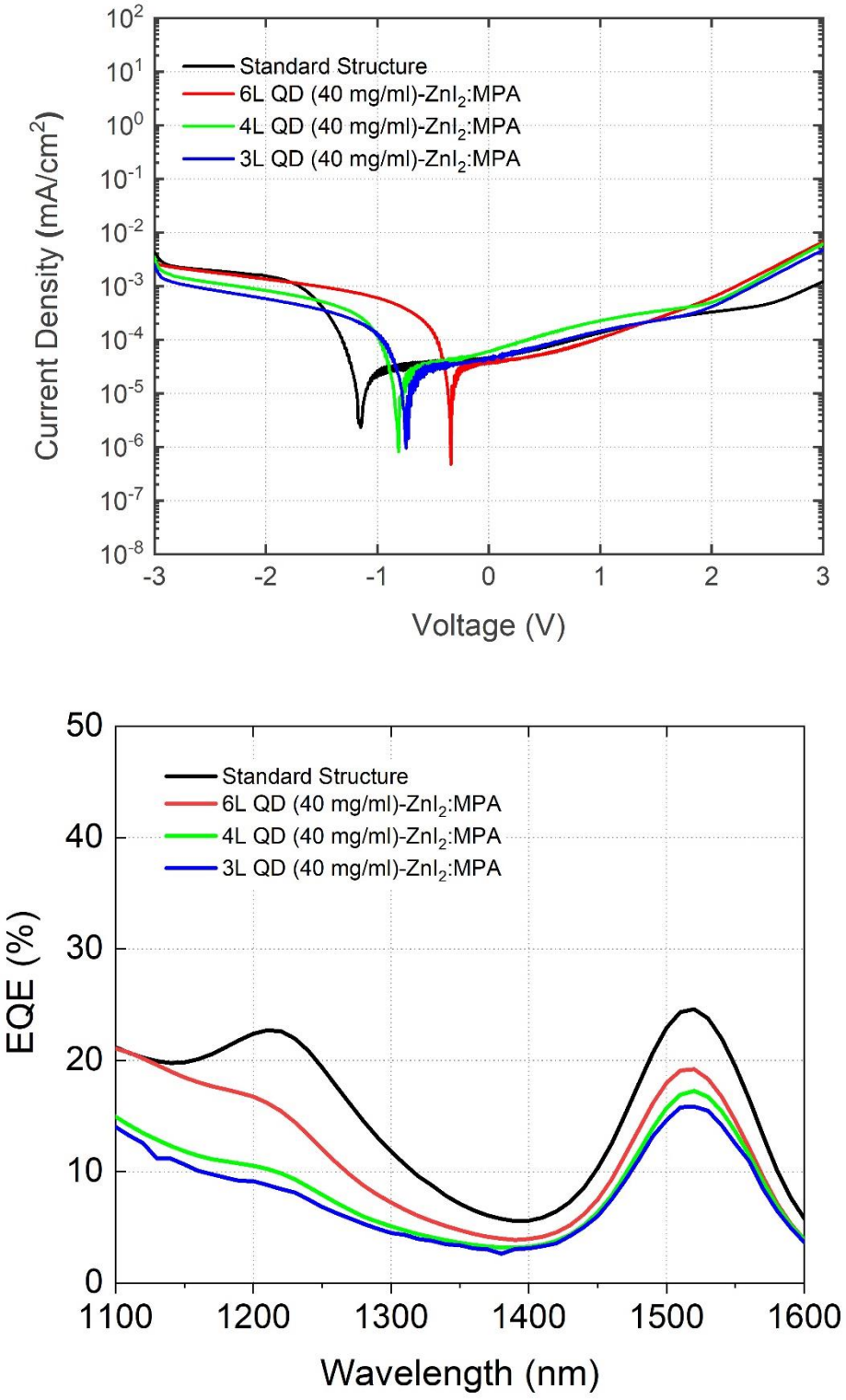

Figure 5. 15 JV (a) and EQE-Wavelength (b) curves comparison for the samples with different thinkesses of QD-ZnI_2:MPA layer.

Silicon substrate with Cu bottom contact was also tested. Figure 5.16 shows the structure of the tested devices.

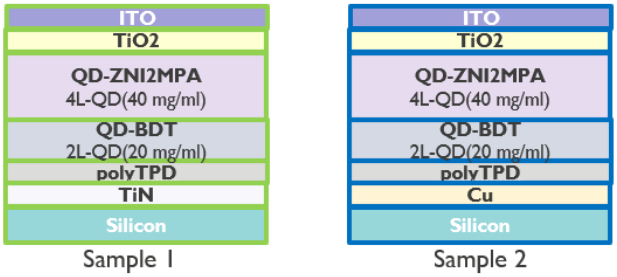

Figure 5. 16 Device structures on silicon substrates which have different contact materials

As shown at figure 5.16a, the device on silicon substrate that has Cu bottom contact shows higher forward current than the device on silicon substrate that has TiN bottom contact. However, both of the devices demonstrate nearly the same dark current values. In addition, the device with Cu contact shows higher EQE value (figure 5.16b). Because Cu is much more reflective than TiN. This allows light that was not absorbed in the first pass to be able to be absorbed again by reflection.

5.5.2 Antireflection Layer Coating

Thinning absorber layers has advantages like easy and cheap production. However, because of the optical interference and limited light absorption, thickness of the absorber layer has a direct effect on EQE. Therefore, to compensate EQE, we deposited an antireflection layer on the top of ITO to be able to increase the absorption by changing the total thickness of the stack to create an optical interference. Here, MoO_x was used as an antireflection layer material, because of its high refractive index value ($n_{MoOx} \approx 2$) [46]. For high reflection, the difference between the medium of the light (air in this study) and the antireflection layer should be as high as possible. The full stack was simulated by using a simulation program to find out the best thickness value for the antireflection layer for the highest yield from the device.

y, the device on silicon substrate with TiN bottom contact was simulated as shown in the figure 5.17. After the simulation of the stack which has 2 layers of QD

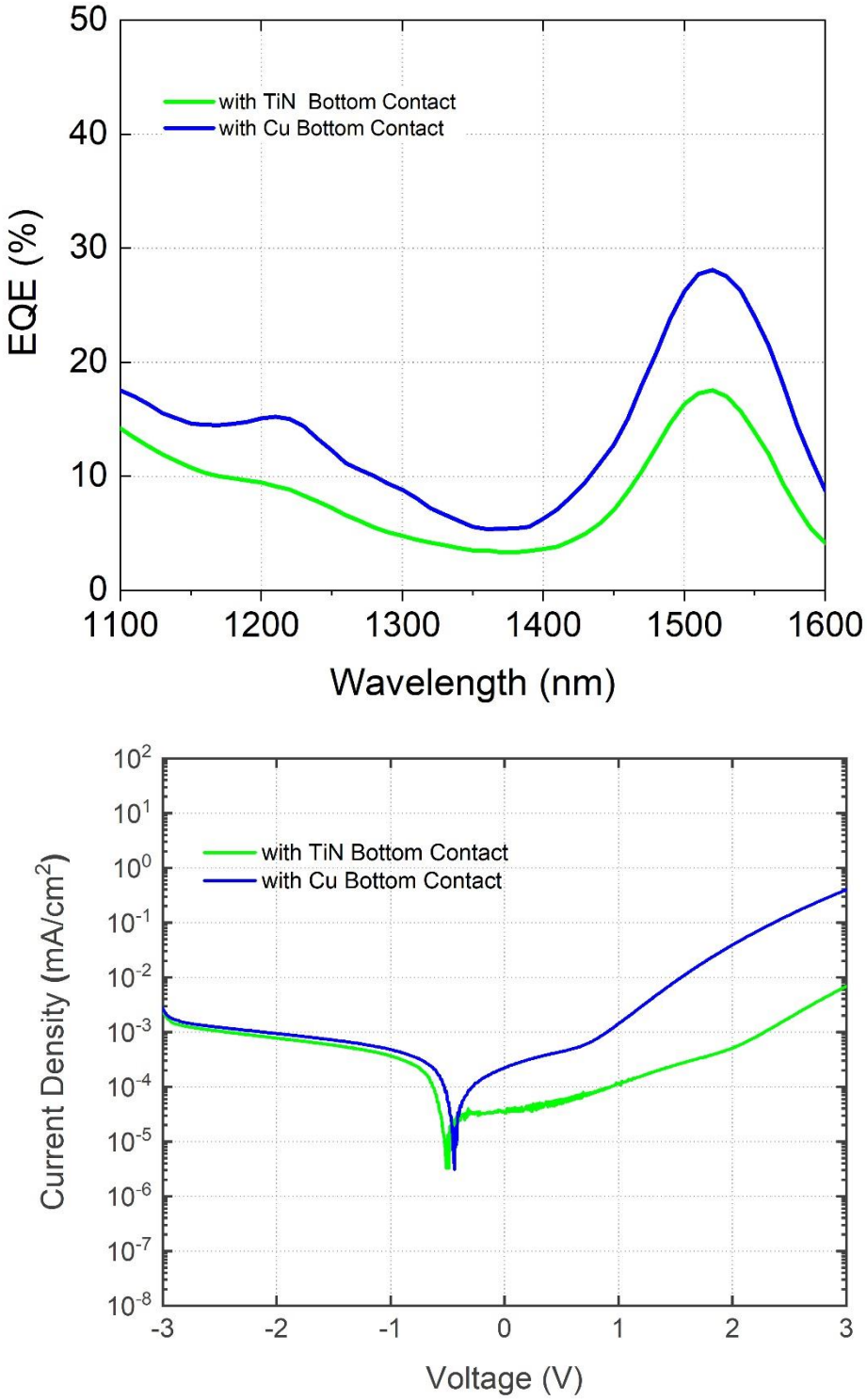

Figure 5. 14 JV (a) and EQE-Wavelength (b) curves comparison for the sample 1 and sample 2

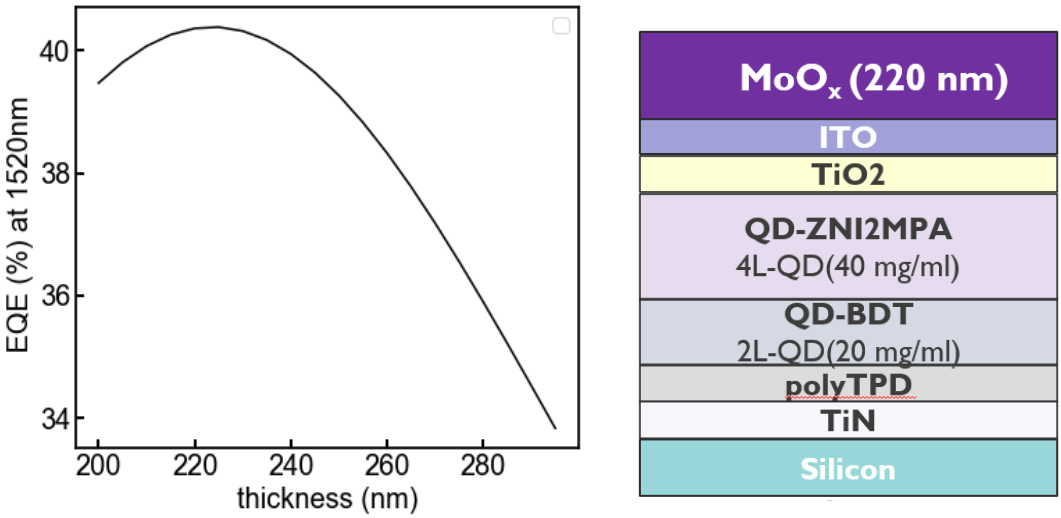

Figure 5. 15 Simulated EQE value for the device which includes antireflection layer (a) device structure after antireflection layer deposition (b)

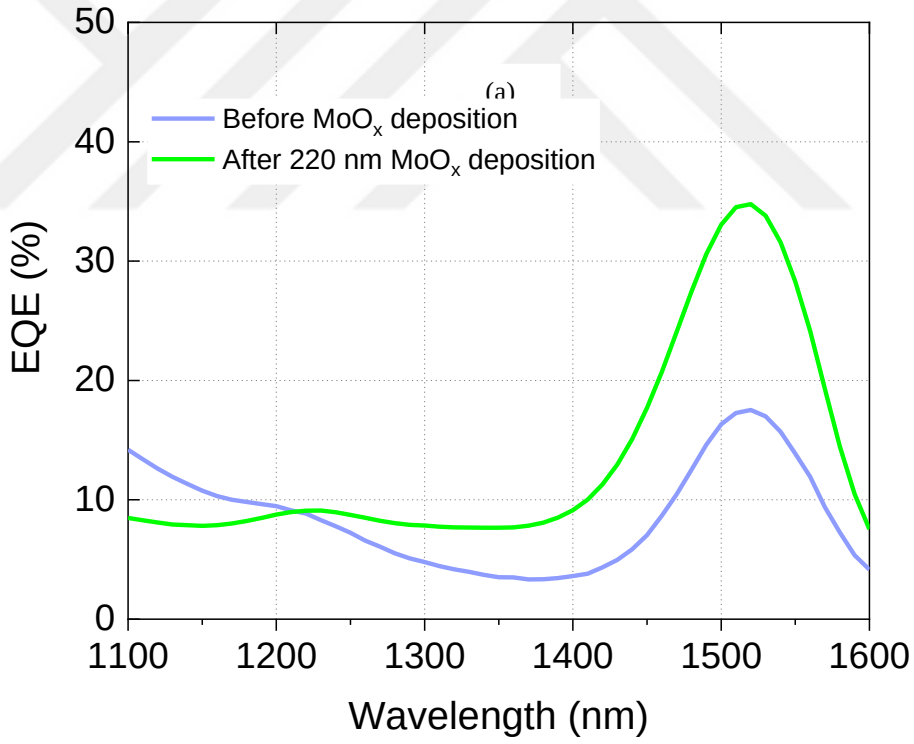

Figure 5.19 Experimental result of EQE after the antireflection layer application

(20 mg/ml)-BDT and 4 layers of QD (40 mg/ml)-ZnI_2:MPA, it was observed from the graph that depositing around 220 nm of MoO_x results in thee shows the highest EQE value.

(b)

Figure 5.18 shows the comparison of the experimental result of EQE before and after MoO_x deposition. Before MoO_x deposition, the device shows around 17% of EQE. However, after antireflection layer deposition, it is observable that there is a good improvement in EQE value from around 17% to around 35%.

Furthermore, different thickness values of QD-ZnI2:MPA layer by changing the number of coating steps were tried. One of the samples has 6 layers of QD (40 mg/ml)-ZnI2:MPA and the other one has 3 layers of QD (40 mg/ml)-ZnI_2:MPA in this experiment. For both of the samples QD-BDT layer is with the same values, 2 layers QD (20 mg/ml)-BDT (figure 5.20).

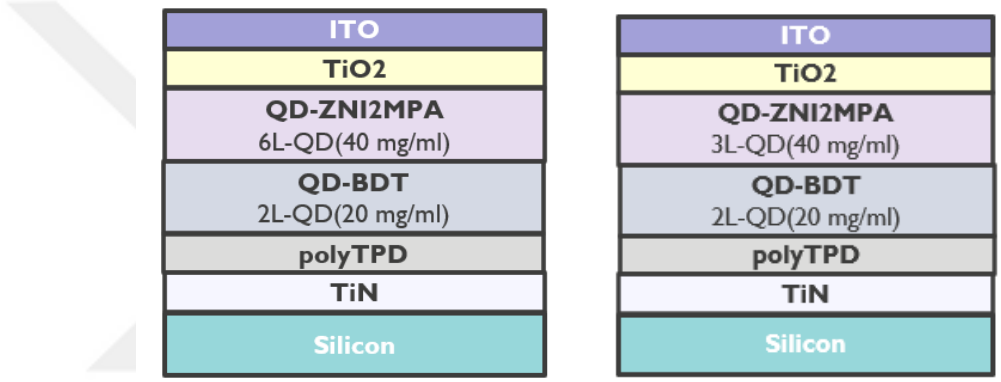

Figure 5.20 Device structures on silicon substrates which have different number of layers for QD-ZnI_2:MPA.

After simulating the each of the devices, optimum values for the MoO_x layer were found. MoO_x layers were coated on the devices in the thickness values of 290 nm and 140 nm for the that has 6 layers of QD (40 mg/ml)-ZnI_2:MPA and the one that has 3 layers of QD (40 mg/ml)-ZnI_2:MPA, respectively.

As shown in figure 5.21, there is an improvement in EQE value from around 17% to around 32% after 290 nm of MoO_x layer deposition for the sample with 6 layers of QD (40 mg/ml)-ZnI_2:MPA. Furthermore, for the sample with 3 layers of QD (40 mg/ml)-ZnI_2:MPA shows an improvement in EQE value from 28% to 38% after 140 nm of MoO_x layer deposition.

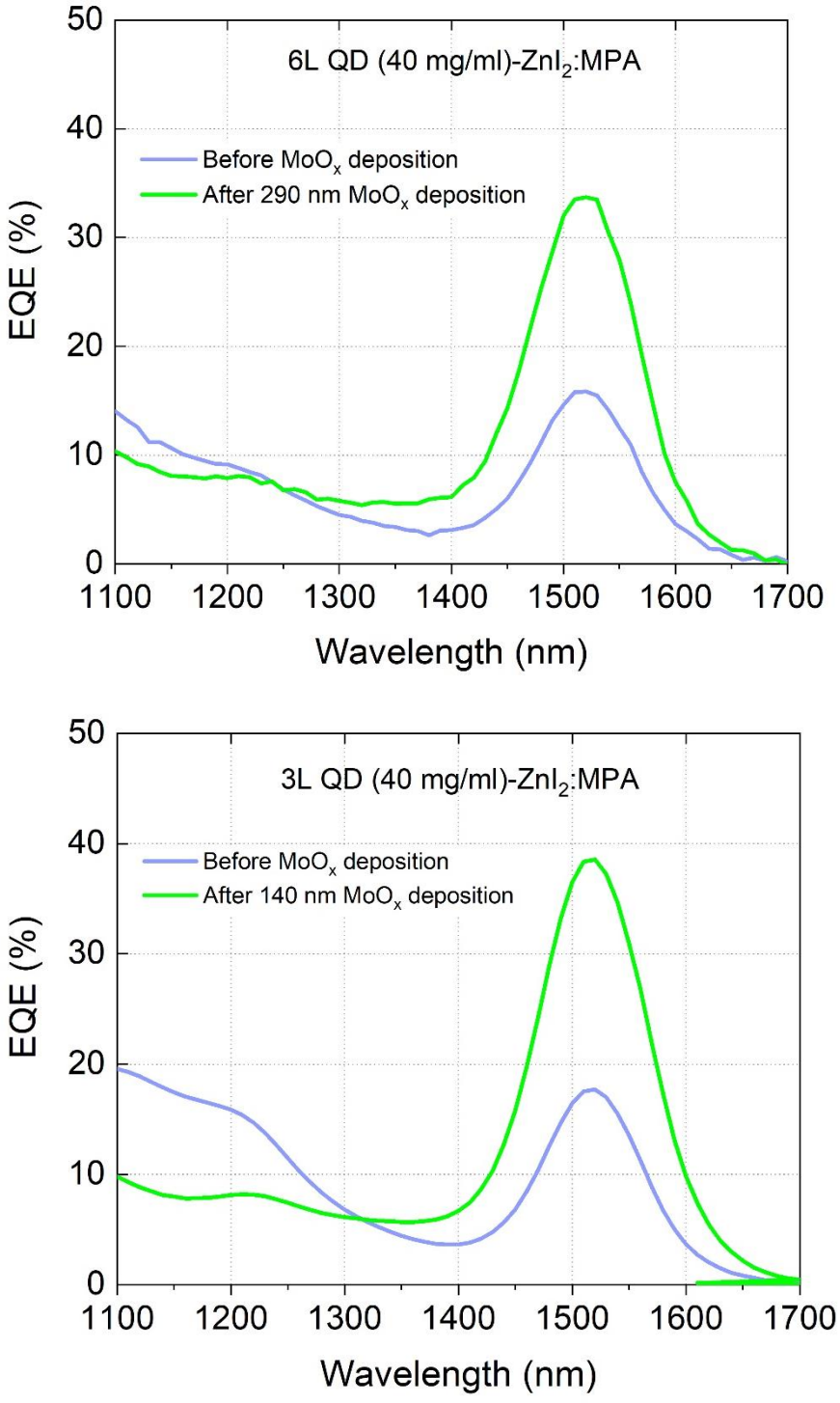

Figure 5.21 Experimental EQE results of the devices with different number of layers for QD-ZnI_2:MPA.

In addition to the experiments with the samples which have TiN bottom contact, we tried antireflection layer coating for the devices that have Cu bottom contact. The effect of the antireflection layer between on the devices with Cu bottom was observed.

Figure 5.22 shows the simulation graph of the device that has 2 layers of QD (20 mg/ml)-BDT and 4 layers of QD (40 mg/ml)-ZnI_2:MPA with Cu bottom contact. It is noticable that the device has the highest EQE value at around 250 nm of thickness values. Figure 1 shows the comparison of the device before and after 250 nm of MoO_x antireflection layer coating. There is an improvement in EQE value from 38% to 45%. However, it is observable that the EQE value of the device with Cu bottom contact is not close to its simulated value unlike the device with TiN bottom contact.

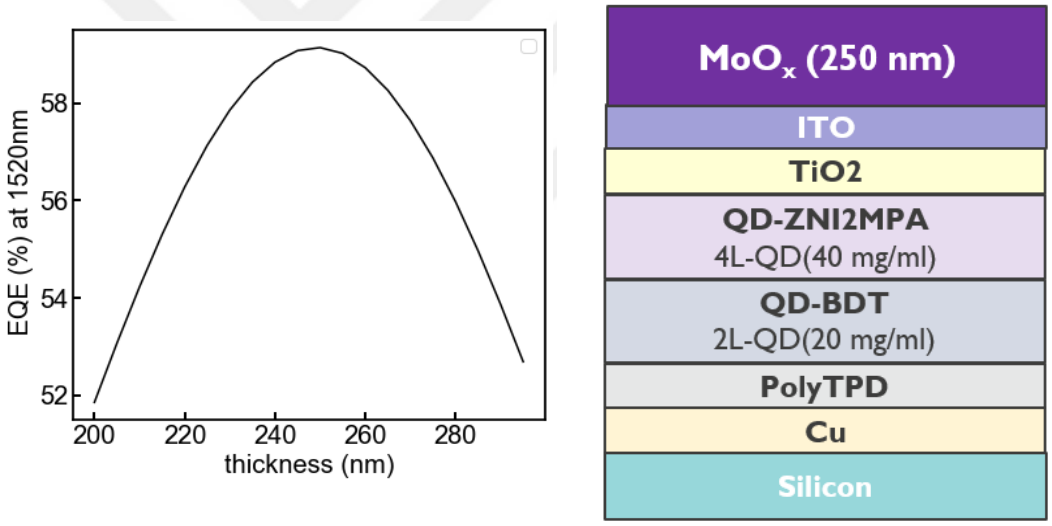

Figure 5.22 Experimental EQE results of the devices with different number of layers for QD-ZnI_2:MPA.

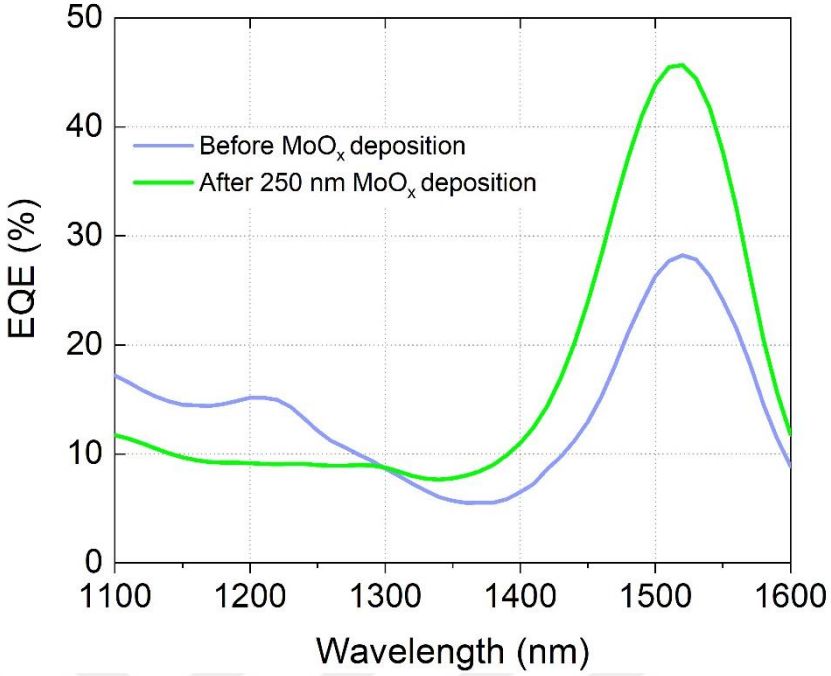

Figure 5.23 Experimental EQE results of the device before and after MoO_X deposition

CHAPTER 6

CONCLUSIONS

The research study carried out in this thesis was conducted within the scope of the projects of the Thin Film Photodetector (TFPD) group of IMEC Belgium for the optimization of quantum dot based thin-film SWIR photodetectors. SWIR imaging can be useful in a variety of situations. For example, chemical detection is possible due to their different spectral features in SWIR. Furthermore, SWIR imaging quite beneficial for tissue analysis. Additionally, due to its extended wavelength, SWIR light scatters less in the atmosphere, resulting in better penetration. However, because silicon's absorption coefficient drops dramatically beyond 1100 nm, imaging in the SWIR needs the use of different materials to be incorporated onto silicon. Colloidal quantum dots (CQDs) may be applied on silicon by using cost-effective and easy solution-based fabrication procedures as an alternative to traditional materials that need high-temperature epitaxial growth [4, 47, 48, 6].

In this thesis, a certain number of experiments were done to reduce the dark current and improve the EQE of the device that is designed already. The main aim is by improving the performance of the devices, enable them to be used as QD SWIR imagers in industry in the future. Various materials were tested on the devices as the transport layer. The reason for focusing on the conduction layers to increase the performance of the device is to prevent dark current by adjusting the energy band alignment of the materials that are used in the device structure and to ensure the maximum number of carriers collected at the contacts. The conductivity of ZnO:Mg used as ETL increased after exposure to UV light. Furthermore, the EQE of C_{60}, another material used as ETL, increased after its thickness decreased. Also, BCP was used as a buffer layer between C60 and metal contact for the first time in a photodetector structure. It was observed that the conductivity increased with the use of C_{60} together with BCP as a buffer layer. Moreover, dark current decrease slightly. As a result of the ETL studies, it was observed that the materials used needed more optimization in order to be able to use them in the photodetector structure.

Some experiments were also done on HTL materials. After NiO_x application, high forward current and high EQE were observed. However, NiO_x shows higher dark current, and it needs higher voltage value for reaching the maximum EQE. Moreover, 2PACz was tried in the structure for the first time in literature. 2PACz is a promising material with its high forward current, high EQE and comparable dark current value.

As a last stage, experiments on thinning the absorber layer were conducted in order to ease fabrication and reduce the fabrication costs. The low EQE caused by the thin absorber layer is compensated by an antireflective layer coating. The thickness of the active layer was adjusted by simulation. However, a significant increase in EQE was observed after the application of the antireflective layer.

For further optimization of the device, transport layer thicknesses can be changed to find the optimal thickness values. Furthermore, studies on ligands, which occupy the most important place in charge conduction, can be done. Different ligand molecules with different concentrations may boost the performance of the devices. All in all, the results of this thesis investigations may open the path for the advancement for industrialization of the imaging technologies.

REFERENCES

[1] J. Peckham, S. O'young, and J. T. Jacobs, "COMPARISON OF MEDIUM AND LONG WAVE INFRARED IMAGING FOR OCEAN BASED SENSING," 2015.

[2] C. L. Tan and H. Mohseni, "Emerging technologies for high performance infrared detectors," *Nanophotonics*, vol. 7, no. 1. Walter de Gruyter GmbH, pp. 169–197, Jan. 01, 2018. doi: 10.1515/nanoph-2017-0061.

[3] F. Nicolo and N. A. Schmid, "Long range cross-spectral face recognition: Matching SWIR against visible light images," *IEEE Transactions on Information Forensics and Security*, vol. 7, no. 6, pp. 1717–1726, 2012, doi: 10.1109/TIFS.2012.2213813.

[4] J. R. Chen, P. C. P. Chao, C. H. Tsai, and W. D. Chen, "Design and realization of a high resolution (640 × 480) SWIR image acquisition system," in *Microsystem Technologies*, 2014, vol. 20, no. 8–9, pp. 1583–1595. doi: 10.1007/s00542-014-2179-7.

[5] L. Zheng *et al.*, "Ambipolar Graphene–Quantum Dot Phototransistors with CMOS Compatibility," *Advanced Optical Materials*, vol. 6, no. 23, Dec. 2018, doi: 10.1002/adom.201800985.

[6] P. E. Malinowski *et al.*, "Thin-film quantum dot photodiode for monolithic infrared image sensors," *Sensors (Switzerland)*, vol. 17, no. 12, Dec. 2017, doi: 10.3390/s17122867.

[7] J. W. Lee, D. Y. Kim, and F. So, "Unraveling the gain mechanism in high performance solution-processed PbS infrared PIN photodiodes," *Advanced Functional Materials*, vol. 25, no. 8, pp. 1233–1238, Feb. 2015, doi: 10.1002/adfm.201403673.

[8] S. Manda *et al.*, “High-definition Visible-SWIR InGaAs Image Sensor using Cu-Cu Bonding of III-V to Silicon Wafer.,” in *Technical Digest - International Electron Devices Meeting, IEDM*, Dec. 2019, vol. 2019-December. doi: 10.1109/IEDM19573.2019.8993432.

[9] S. Masala *et al.*, “The Silicon:Colloidal Quantum Dot Heterojunction,” *Advanced Materials*, vol. 27, no. 45, pp. 7445–7450, Dec. 2015, doi: 10.1002/adma.201503212.

[10] X. Yin, C. Zhang, Y. Guo, Y. Yang, Y. Xing, and W. Que, “PbS QD-based photodetectors: Future-oriented near-infrared detection technology,” *Journal of Materials Chemistry C*, vol. 9, no. 2, pp. 417–438, Jan. 2021, doi: 10.1039/d0tc04612d.

[11] F. Yang *et al.*, “Highly Enhanced SWIR Image Sensors Based on Ge 1- x Sn x -Graphene Heterostructure Photodetector,” *ACS Photonics*, vol. 6, no. 5, pp. 1199–1206, May 2019, doi: 10.1021/acsphotonics.8b01731.

[12] K. Xu, W. Zhou, and Z. Ning, “Integrated Structure and Device Engineering for High Performance and Scalable Quantum Dot Infrared Photodetectors,” *Small*, vol. 16, no. 47. Wiley-VCH Verlag, Nov. 01, 2020. doi: 10.1002/smll.202003397.

[13] A. Chilvery, S. Das, P. Guggilla, C. Brantley, and A. Sunda-Meya, “A perspective on the recent progress in solution-processed methods for highly efficient perovskite solar cells,” *Science and Technology of Advanced Materials*, vol. 17, no. 1. Taylor and Francis Ltd., pp. 650–658, Jan. 01, 2016. doi: 10.1080/14686996.2016.1226120.

[14] J. Kim, S. Song, Y.-H. Kim, and S. K. Park, “Recent Progress of Quantum Dot-Based Photonic Devices and Systems: A Comprehensive Review of Materials, Devices, and Applications,” *Small Structures*, vol. 2, no. 3, p. 2000024, Mar. 2021, doi: 10.1002/sstr.202000024.

[15] W. Chen, D. Qi, X. Gao, and A. T. S. Wee, “Surface transfer doping of semiconductors,” *Progress in Surface Science*, vol. 84, no. 9–10. pp. 279–321, Sep. 2009. doi: 10.1016/j.progsurf.2009.06.002.

[16] D. A. Neamen, *Semiconductor physics and devices : basic principles*. McGraw-Hill, 2012.

[17] J. U. Lee, P. P. Gipp, and C. M. Heller, “Carbon nanotube p-n junction diodes,” *Applied Physics Letters*, vol. 85, no. 1, pp. 145–147, Jul. 2004, doi: 10.1063/1.1769595.

[18] R. Saran and R. J. Curry, “Lead sulphide nanocrystal photodetector technologies,” *Nature Photonics*, vol. 10, no. 2. Nature Publishing Group, pp. 81–92, Feb. 01, 2016. doi: 10.1038/nphoton.2015.280.

[19] A. H. Howlader, F. Li, and R. Zheng, “Carbon Nanomaterials for Halide Perovskites-Based Hybrid Photodetectors,” *Advanced Materials Technologies*, vol. 5, no. 12. Wiley-Blackwell, Dec. 01, 2020. doi: 10.1002/admt.202000643.

[20] P. V. K. Yadav, B. Ajitha, Y. A. Kumar Reddy, and A. Sreedhar, “Recent advances in development of nanostructured photodetectors from ultraviolet to infrared region: A review,” *Chemosphere*, vol. 279, Sep. 2021, doi: 10.1016/j.chemosphere.2021.130473.

[21] K. M. Gupta and N. Gupta, “Engineering Materials Advanced Semiconducting Materials and Devices.” [Online]. Available: http://www.springer.com/series/4288

[22] X. Jianggwu and Z. M. Wanggeditors, “Quantum Dot Photodetectors.” [Online]. Available: http://www.springer.com/series/7544

[23] M. Cabrera, “Development of 15 Micron Cutoo Wavelength HgCdTe Detector Arrays for Astronomy.” [Online]. Available: http://www.springer.com/series/8790

[24] R. Hui, “Photodetectors,” in *Introduction to Fiber-Optic Communications*, Elsevier, 2020, pp. 125–154. doi: 10.1016/b978-0-12-805345-4.00004-4.

[25] W. Yang, J. Chen, Y. Zhang, Y. Zhang, J. H. He, and X. Fang, “Silicon-Compatible Photodetectors: Trends to Monolithically Integrate Photosensors with Chip Technology,” *Advanced Functional Materials*, vol. 29, no. 18. Wiley-VCH Verlag, May 02, 2019. doi: 10.1002/adfm.201808182.

[26] X. Jianggwu and Z. M. Wanggeditors, “Quantum Dot Photodetectors.” [Online]. Available: http://www.springer.com/series/7544

[27] E. Georgitzikis, “Infrared Sensitive Thin-Film Photodetectors for Integration on Top of CMOS.”

[28] Y. Cho *et al.*, “Balancing Charge Carrier Transport in a Quantum Dot P-N Junction toward Hysteresis-Free High-Performance Solar Cells,” *ACS Energy Letters*, vol. 3, no. 4, pp. 1036–1043, Apr. 2018, doi: 10.1021/acsenergylett.8b00130.

[29] C. H. M. Chuang, P. R. Brown, V. Bulović, and M. G. Bawendi, “Improved performance and stability in quantum dot solar cells through band alignment engineering,” *Nature Materials*, vol. 13, no. 8, pp. 796–801, 2014, doi: 10.1038/nmat3984.

[30] V. Pejović, “P-N Junction Optimization in PbS Quantum Dot Based Infrared Thin-Film Photodetectors,” 2018.

[31] J. P. Clifford, G. Konstantatos, K. W. Johnston, S. Hoogland, L. Levina, and E. H. Sargent, “Fast, sensitive and spectrally tuneable colloidal-quantum-dot photodetectors,” *Nature Nanotechnology*, vol. 4, no. 1, pp. 40–44, 2009, doi: 10.1038/nnano.2008.313.

[32] J. R. Manders *et al.*, “Low-noise multispectral photodetectors made from all solution-processed inorganic semiconductors,” *Advanced Functional Materials*, vol. 24, no. 45, pp. 7205–7210, Dec. 2014, doi: 10.1002/adfm.201402094.

[33] M. Biondi *et al.*, “Control over Ligand Exchange Reactivity in Hole Transport Layer Enables High-Efficiency Colloidal Quantum Dot Solar Cells,” *ACS Energy Letters*, vol. 6, no. 2, pp. 468–476, Feb. 2021, doi: 10.1021/acsenergylett.0c02500.

[34] O. Voznyy, D. Zhitomirsky, P. Stadler, Z. Ning, S. Hoogland, and E. H. Sargent, “A charge-orbital balance picture of doping in colloidal quantum dot solids,” *ACS Nano*, vol. 6, no. 9, pp. 8448–8455, Sep. 2012, doi: 10.1021/nn303364d.

[35] S. Pradhan, A. Stavrinadis, S. Gupta, Y. Bi, F. di Stasio, and G. Konstantatos, “Trap-State Suppression and Improved Charge Transport in PbS Quantum Dot Solar Cells with Synergistic Mixed-Ligand Treatments,” *Small*, vol. 13, no. 21, Jun. 2017, doi: 10.1002/smll.201700598.

[36] S. Y. Jeong *et al.*, “High-Speed Colloidal Quantum Dot Photodiodes via Accelerating Charge Separation at Metal–Oxide Interface,” *Small*, vol. 15, no. 13, Mar. 2019, doi: 10.1002/smll.201900008.

[37] J. H. Kim *et al.*, “Performance improvement of quantum dot-light-emitting diodes enabled by an alloyed ZnMgO nanoparticle electron transport layer,” *Chemistry of Materials*, vol. 27, no. 1, pp. 197–204, Jan. 2015, doi: 10.1021/cm503756q.

[38] J. Choi *et al.*, “Activated Electron-Transport Layers for Infrared Quantum Dot Optoelectronics,” *Advanced Materials*, vol. 30, no. 29, Jul. 2018, doi: 10.1002/adma.201801720.

[39] X. Guo, G. Luo, J. Liu, C. Liao, G. Wang, and S. Li, “A 16.5% efficient perovskite solar cells with inorganic NiO film as hole transport material,” *IEEE Journal of Photovoltaics*, vol. 8, no. 4, pp. 1039–1043, Jul. 2018, doi: 10.1109/JPHOTOV.2018.2825228.

[40] A. Magomedov *et al.*, “Self-Assembled Hole Transporting Monolayer for Highly Efficient Perovskite Solar Cells,” *Advanced Energy Materials*, vol. 8, no. 32, Nov. 2018, doi: 10.1002/aenm.201801892.

[41] Y. Lin *et al.*, “18.4 % Organic Solar Cells Using a High Ionization Energy Self-Assembled Monolayer as Hole-Extraction Interlayer,” *ChemSusChem*, vol. 14, no. 17, pp. 3569–3578, Sep. 2021, doi: 10.1002/cssc.202100707.

[42] W. K. Koh, S. Park, and Y. Ham, “Phosphonic Acid Stabilized Colloidal CsPbX3 (X=Br, I) Perovskite Nanocrystals and Their Surface Chemistry,” *ChemistrySelect*, vol. 1, no. 13, pp. 3479–3482, Aug. 2016, doi: 10.1002/slct.201600809.

[43] Y. Hou *et al.*, “Suppression of Hysteresis Effects in Organohalide Perovskite Solar Cells,” *Advanced Materials Interfaces*, vol. 4, no. 11, Jun. 2017, doi: 10.1002/admi.201700007.

[44] M. S. Islam, “Analytical modeling of organic solar cells including monomolecular recombination and carrier generation calculated by optical transfer matrix method,” *Organic Electronics*, vol. 41, pp. 143–156, Feb. 2017, doi: 10.1016/j.orgel.2016.10.040.

[45] E. Georgitzikis *et al.*, “Integration of PbS Quantum Dot Photodiodes on Silicon for NIR Imaging,” in *IEEE Sensors Journal*, Jul. 2020, vol. 20, no. 13, pp. 6841–6848. doi: 10.1109/JSEN.2019.2933741.

[46] N. Miyata, T. Suzuki, and R. Ohyama, “Physical properties of evaporated molybdenum oxide films,” *Thin Solid Films*, vol. 281–282, no. 1–2, pp. 218–222, Aug. 1996, doi: 10.1016/0040-6090(96)08617-8.

[47] L. Lv *et al.*, “Flexible Short-Wave Infrared Image Sensors Enabled by High-Performance Polymeric Photodetectors,” *Macromolecules*, vol. 53, no. 23, pp. 10636–10643, Dec. 2020, doi: 10.1021/acs.macromol.0c01988.

[48] Q. Xu, I. T. Cheong, L. Meng, J. G. C. Veinot, and X. Wang, “Silicon Surface Passivation for Silicon-Colloidal Quantum Dot Heterojunction Photodetectors,” *ACS Nano*, vol. 15, no. 11, pp. 18429–18436, Nov. 2021, doi: 10.1021/acsnano.1c08002.

CURRICULUM VITAE

PERSONAL INFORMATION

Name Surname **:** Irem SUTCU

Date of Birth **:**

Phone **:**

E-mail **:**

EDUCATION

High School **:** Meliha Hasanali Bostan Cubuk Science High School (2008-2012

Bachelor **:** Ankara Yıldırım Beyazıt University, Metallurgy and Materials Engineering (2012-2018)

Master Degree **:** Ankara Yıldırım Beyazıt University, Energy Systems Engineering (2019-2022)

EXPERIANCES

IMEC Leuven (Belgium)– International Scholar, Quantum Dot Based Thin Film Photodetectors (02.08.21-15.06.22)

PUBLICATIONS-SCI

Atli, A.; Sutcu, I.; Yildiz, ZK.; Yildiz, A. "Optimizing Deposition Parameters of DSSCs Composed of Blue TiO_2" IEEE Journal of Photovoltaics 11 (1), 118-123 (2020)

CONFERENCE PROCEEDINGS

Sutcu, A. Atli, A. Atilgan, A. Yildiz, ‘’Performance Improvement of DSSCs by Photoanode Treatments’’ 5th International Conferences on Engineering Sciences (Ankara, Turkey), (2019)

Sutcu, I. Pejovic V., Lieberman, I. Lim, M.J. Georgitzikis, E. Malinowski, P Cheyns, D. Celebi, N. Salimi, K.“Performance Improvement in Quantum Dot Thin Film Photodetectors via C_{60}-BCP Electron Transport Layers” 6th Ankara International Congress on Scientific Research (Ankara, Turkey), (2022)